



HAL
open science

Field deployment and analysis of hydraulic tomography experiments with periodic slug tests in an anisotropic littoral aquifer

Aymen Nefzi, Daniel Paradis, René Lefebvre, Olivier Bour, Nicolas Lavenant

► **To cite this version:**

Aymen Nefzi, Daniel Paradis, René Lefebvre, Olivier Bour, Nicolas Lavenant. Field deployment and analysis of hydraulic tomography experiments with periodic slug tests in an anisotropic littoral aquifer. *Journal of Hydrology*, 2025, 653, pp.132747. 10.1016/j.jhydrol.2025.132747 . insu-04918220

HAL Id: insu-04918220

<https://insu.hal.science/insu-04918220v1>

Submitted on 29 Jan 2025

HAL is a multi-disciplinary open access archive for the deposit and dissemination of scientific research documents, whether they are published or not. The documents may come from teaching and research institutions in France or abroad, or from public or private research centers.

L'archive ouverte pluridisciplinaire **HAL**, est destinée au dépôt et à la diffusion de documents scientifiques de niveau recherche, publiés ou non, émanant des établissements d'enseignement et de recherche français ou étrangers, des laboratoires publics ou privés.

Journal Pre-proofs

Field deployment and analysis of hydraulic tomography experiments with periodic slug tests in an anisotropic littoral aquifer

Aymen Nefzi, Daniel Paradis, René Lefebvre, Olivier Bour, Nicolas Lavenant

PII: S0022-1694(25)00085-X
DOI: <https://doi.org/10.1016/j.jhydrol.2025.132747>
Reference: HYDROL 132747

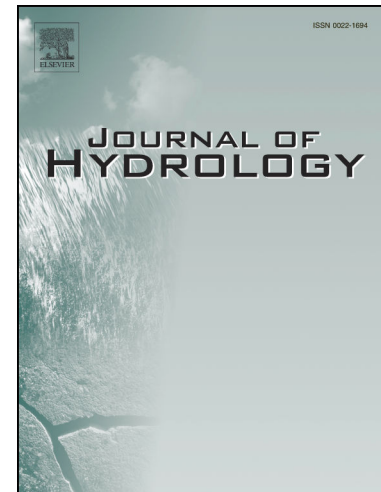
To appear in: *Journal of Hydrology*

Received Date: 15 April 2024
Revised Date: 31 December 2024
Accepted Date: 13 January 2025

Please cite this article as: Nefzi, A., Paradis, D., Lefebvre, R., Bour, O., Lavenant, N., Field deployment and analysis of hydraulic tomography experiments with periodic slug tests in an anisotropic littoral aquifer, *Journal of Hydrology* (2025), doi: <https://doi.org/10.1016/j.jhydrol.2025.132747>

This is a PDF file of an article that has undergone enhancements after acceptance, such as the addition of a cover page and metadata, and formatting for readability, but it is not yet the definitive version of record. This version will undergo additional copyediting, typesetting and review before it is published in its final form, but we are providing this version to give early visibility of the article. Please note that, during the production process, errors may be discovered which could affect the content, and all legal disclaimers that apply to the journal pertain.

© 2025 Published by Elsevier B.V.



Field deployment and analysis of hydraulic tomography experiments with periodic slug tests in an anisotropic littoral aquifer

Aymen Nefzi¹, Daniel Paradis^{1,2}, René Lefebvre¹, Olivier Bour³ & Nicolas Lavenant³

¹ Centre Eau Terre Environnement (INRS-ETE) - Institut national de la recherche scientifique, Québec, Canada

² Ressources Naturelles Canada - Commission géologique du Canada, Québec, Canada

³ Université Rennes, CNRS, Géosciences Rennes, UMR 6118, 35000 Rennes, France

1. Introduction

The heterogeneity of hydraulic properties in aquifers plays a crucial role in controlling groundwater flow (e.g. Frei et al., 2009; Yetbarek et al., 2020; Zeyrek et al., 2023; Chen et al., 2023) and influences processes such as solute transport and dispersivity (e.g. Leblanc et al., 1991; Boggs et al., 1992; Sudicky and Illman, 2011; Hoque and Burgess, 2020; Yin et al., 2023). Accurately mapping this heterogeneity remains an ongoing challenge that requires continuous development of field methods (de Marsily et al., 2005).

Several field methods have been developed to estimate hydraulic properties along wells, especially hydraulic conductivity (K). These methods usually require tests at small intervals to capture vertical variations of K . The most common method is to use inflatable packers to isolate discrete intervals (deca-metric to sub-metric) along open holes or screened wells and perform slug tests or pumping tests. In a slug test, a known volume of water is instantaneously withdrawn or injected into the well (e.g., Rehfeldt et al., 1992; Ross and McElwee, 2007), whereas in pumping tests, water is withdrawn or injected at a constant rate (e.g., Lancaster-Jones, 1975; Price et al., 1982; Quinn et al., 2011). In these tests, the changes in head over time in response to the hydraulic stimulation are measured and evaluated using analytical or numerical methods (e.g., Kruseman and de Ridder, 2000). Flowmeter tests are another technique that has been used to obtain vertical profiles of transmissivity (T) (e.g., Morin et al., 1988; Molz et al., 1989; Hanson and Nishikawa, 1996; Paillet, 1998; Crisman et al., 2001; Paradis et al., 2011). Flowmeters use impellers, heat pulses, or electromagnetic devices to measure flow rates at discrete intervals along a well during pumping. Recent advances include FLUTE tests, which involve deploying a flexible liner into an open well under a controlled driving head. By measuring the rate of descent of the liner, the test can profile the transmissivity (T) of the well (e.g., Keller et al., 2014; Quinn et al., 2015). Slug tests and permeameter tests have been adapted for use with direct-push equipment (e.g., Butler et al., 2007; Dietrich et al., 2008; Liu et al., 2009). In these methods, a system of casing and screen is driven

into unconsolidated sediments to the desired depths to perform tests. This approach allows for very fine vertical resolution of K , often in the centimeter range.

While 1D profiles are invaluable in identifying vertical variations in hydraulic properties at individual wells, mapping heterogeneity between these wells is better assessed by inter-well interference tests, such as hydraulic tomography (Berg and Illman, 2015). Hydraulic tomography is based on inverse modeling of multiple hydraulic tests with head measurements at multiple observation intervals to map 2D or 3D distributions (tomograms) of hydraulic properties (e.g. Bohling, 1993; Tosaka et al., 1993; Gottlieb and Dietrich, 1995). In most field studies using hydraulic tomography, pumping tests were performed at a constant rate to generate a stimulation. When analyzing pumping test tomography, either steady-state shape (e.g., Bohling et al., 2007) or steady-state head (e.g., Li et al., 2008; Cardiff et al., 2009) or full transient responses (e.g., Illman et al., 2009; Berg and Illman, 2011; Cardiff et al., 2012; 2013; Hochstetler et al., 2015; Tiedeman and Barrash, 2020) were used. Few other field applications of hydraulic tomography have relied on slug tests (e.g. Brauchler et al, 2011; 2013; Lochbühler et al, 2013; Paradis et al, 2016; Liu et al, 2023). All these previous studies have shown that the obtained tomograms of hydraulic properties are generally consistent with the geology of the sites or independent profiles of hydraulic conductivity obtained with other techniques along the wells. Some of them also successfully reproduce independent hydraulic tests, suggesting that the spatial structure of the heterogeneity is well reproduced.

The use of hydraulic tomography with periodic signals has also been proposed for the characterization of aquifer heterogeneity. Rosa and Horne (1997) have shown that a periodic square-wave signal, with alternating periods of constant and zero flow rates, can provide more information than a signal generated by a conventional constant-rate pumping test for the same test configuration. The reason for the better performance is that the periodic signal contains multiple sinusoidal components, each of which investigates a different region of the aquifer. Varying the period of a pure sinusoidal signal also allows the investigation of different aquifer regions. Therefore, their combined analysis can possibly improve heterogeneity characterization (Black and Kipp, 1981; Hollaender et al., 2002; Ahn and Horne, 2010; Cardiff et al., 2013; Paradis et al. 2024).

However, only a few published field applications of periodic hydraulic tomography have revealed its potential for mapping aquifer heterogeneity. Lavenue and Marsilly (2001) performed sinusoidal pumping tests with a single period (72 min) to estimate K of an unconfined dolomite aquifer. Although the recovered model accurately reproduced an independent periodic test used for validation, the information content of the single period was not assessed. Fischer et al. (2018) conducted harmonic pumping tests with two different periods (2 and 5 min) to estimate the transmissivity (T) and the storativity (S) of the conduits and the matrix of a karst network in the horizontal 2D plane. Their results show very different structures of the karst network for each period, which was attributed to the relative change in the induced flow field for each period. Fischer et al. (2020) also mapped the heterogeneity of an alluvial aquifer using oscillatory pumping tests

with two different periods (5 and 10 min). The resulting maps of T and S values, averaged over 2D depth, for the separate and joint inversions of the two periods differed only slightly and were all consistent with the geology and contamination history of the site (Fischer et al., 2020). However, they concluded that a joint inversion with the two periods “provided more information on the heterogeneous distribution of the field properties” based on the analysis of the uncertainty maps of the separate and joint inversions. Finally, Cardiff et al. (2020) reported on a field application of oscillatory hydraulic tomography with a series of periods ranging between 5 and 70 seconds in a fluvial aquifer. Data from all periods were inverted together to reconstruct the 3D K -field (S_s was fixed). This joint inversion reveals a strong positive correlation with K profiles obtained by slug tests. However, a rather moderate correlation with tomograms obtained by constant pumping rate tomography from a previous study was found.

While this review highlights successful applications of hydraulic tomography with periodic signals, none of them considered the anisotropy in K (or the ratio of vertical (K_v) to horizontal (K_h) hydraulic conductivity, K_v/K_h). K_v/K_h expresses the effects of small-scale heterogeneity in K at a larger scale and controls groundwater flow and solute transport at different scales (e.g. Hart et al. 2006; Barry et al. 2009; Falta et al. 2005). According to Shepley (2024), K_v tend to be overestimated in groundwater models due to a general lack of knowledge about this hydraulic parameter. The aim of this paper is to provide a practical example of hydraulic tomography with periodic tests considering K_v/K_h . The examination of new applications is crucial to understand the benefits of this method and to identify opportunities for improvement. This includes the entire process, from field methods to data processing techniques and data inversion procedures. This study therefore presents the field experimentation and analysis of such an experiment conducted in a littoral aquifer at the St-Lambert Test Site in Canada. This site is known for its strong contrasts between K_v and K_h , reaching up to two orders of magnitude on a decimetric scale (Paradis and Lefebvre, 2013; Paradis et al., 2014). This highlights the interest in exploring the effectiveness of hydraulic tomography with periodic signals in highly heterogeneous (or anisotropic) aquifers.

In this proof-of-concept experiment on periodic tomography in an anisotropic aquifer, the head responses of a series of 10 periodic slug tests at 0.61-m intervals in a source well are described and analyzed. The head was recorded in the source interval itself and in 3 observation intervals in a nearby well. The periodic signal was generated by the movement of a rod in the source interval, with the amplitude and period numerically controlled by a winch. Three different periods were applied (150, 300 and 600 s). This resulted in 120 (3 periods x 10 tests x 4 intervals) recordings of head responses that could be analyzed. The heterogeneous fields of K_h , K_v/K_h and S_s were estimated by inversion using the Levenberg-Marquardt algorithm in combination with a groundwater flow model accounting for wellbore storage. The tomography experiments with different period were analyzed individually and together. Inverted tomograms were also verified by a cross-verification procedure and the simulation of conventional slug tests carried out in a tomographic arrangement to assess the information content of the different periods. The estimation of K_v/K_h from hydraulic tomography experiment with periodic tests was also explored.

2. Test site

The test site is located at Saint-Lambert-de-Lauzon, 40 km south of Quebec City (Canada). This site has been extensively studied to support the development of varied aquifer characterization techniques (Dubreuil-Boisclair et al., 2011; Gloaguen et al., 2012; Gernez et al., 2019; Paradis and Lefebvre, 2013; Paradis et al., 2011; Paradis et al., 2014; Paradis et al., 2015; Paradis et al., 2016; Ruggeri et al., 2014; Tremblay et al., 2014). The aquifer is made up of unconsolidated Late Quaternary sediments deposited in the Champlain Sea, an arm of the Atlantic Ocean that invaded the St. Lawrence Valley at the end of the last glaciation. Due to the changing energy levels along the (Bolduc, 2003; Parent and Occhietti, 1988) shores of the Champlain Sea, this littoral and sublittoral sedimentary environment is characterized by overlapping thin layers of sand and silt (Figure 1). These sediments typically exhibit poor to very poor grain size sorting and frequent transitions in sediment composition. Figure 2 compares the vertical hydraulic conductivity K_v measured in the lab on 0.15 m long sediment samples to the horizontal hydraulic conductivity K_h obtained from slug tests between packers covering the same intervals. The figure shows that these rapid vertical variations in sediment grain size have led to heterogeneous and severely anisotropic conditions. The values of K_v/K_h for small 0.15 m intervals vary from 1 (isotropic condition) to very anisotropic conditions with values as low as 0.01 (two orders of magnitude difference between K_v and K_h). Previous field tests by Paradis and Lefebvre (2013) and Paradis et al. (2016) have shown that this anisotropy can be estimated using vertical interference tests obtained from slug tests between packers in a single well or between wells in a tomographic configuration. The granular, semi-confined aquifer is up to 20 m thick (12 m at the test site) and has an impermeable base made up of a glaciomarine diamicton. The shallow water table is less than 1 m below the land surface.

Figure 1

Figure 2

3. Test equipment and procedures

3.1. Direct-push wells

Figure 3 shows the spatial arrangement of wells S18 and O21 used for the field experiment. The wells are screened over the entire saturated thickness of the aquifer. They were installed without sand packs (screens in direct contact with the natural sediments) using direct-push equipment according to the protected screen method (Paradis et al., 2011). The diameter of each well is 0.051 m with a screen length of 7.6 m. Before the experiment, the wells were developed with an inertial pump and a surge block to ensure that the screens were free of sediment deposits.

Figure 3

3.2. Packer system and pressure loggers

To increase flexibility in the design of the experiment, inflatable low-pressure packers and screens with threaded tubes were made. This design allows the length of the screens between the packers to be adjusted to accommodate different experimental setups. A double packer arrangement with 0.61 m long packers was used to isolate 0.61 m long source intervals along S18 (Figure 4a). This assembly was connected to the surface via a riser tube into which the periodic source was immersed (see Section 3.3). In O21, an arrangement of four packers was set up to isolate three observation intervals, each 0.30 m long and 0.91 m apart (center to center) (Figure 4a). To reduce data collection time, the packer arrangement in O21 was moved every three tests in S18. After each packer arrangement movement in the source or observation wells, there was a rest period until the head had stabilized.

A network of pressure loggers (Solinst Levelogger 3001 with a scale of 10 m and a resolution of 0.006 m) was installed in the source interval and in the three observation intervals. The logger in the source interval was placed inside the screen (“fixed logger” in Figure 4a) to ensure that the head loss due to turbulence or friction along the riser tube did not affect the measurements (e.g., Hommersen et al., 2021). However, analysis of the heads measured in the source screen together with those measured by another logger at the lower end of the rod (“moving logger” in Figure 4a) revealed no significant head loss. The clocks of the pressure loggers were synchronized at the beginning of each day and a sampling rate of 1 Hz was used to record head data.

Figure 4

3.3. Periodic source

The periodic stimulation was performed with a 2.8 m long aluminum rod immersed in the riser tube. The rod was attached to a winch that was numerically controlled (Figure 4a). Moving the rod upwards is like pumping water out of the riser, whereas lowering the rod is like injecting water. A similar setup was used by Becker and Gultinan (2010) and Gultinan and Becker (2015). The diameter of the rod was chosen to maximize the volume of water displaced for the tests while ensuring that the water could move freely between the rod and the inside of the riser tube (Figure 4b). Before starting a test, the rod was semi-submerged, and a computer program was used to control the amplitude and period of the vertical movement. The amplitude of the rod displacement was adjusted for each test (Table 1) to ensure that the water level fluctuations always occurred within the annular space between the rod and the riser tube (i.e., no dewatering or flooding of the rod). Three different periods were used for the source signal: 150, 300 and 600 s. These periods were chosen to obtain maximum head variations in the observation intervals. The tests were performed by running the three periods in each source interval sequentially, with a rest period between each period. At least three cycles were performed for each period. The displacement of

the rod was monitored and used to calculate the flow induced in the well for each test (see Section 4.4).

3.4. Field experiment description

The entire field experiment consisted of a series of three tomography experiments between S18 and O21 with the three different periods (Figure 3). The distance between the wells is 5.35 m. Each tomography experiment comprised 10 periodic slug tests performed in 8 source intervals in S18, with the head recorded in the source interval itself and in three observation intervals in O21 (Table 1). Source intervals S18.510 and S18.690 in S18 were tested twice with a different configuration of observation intervals in O21. Tests were conducted along S18 at successive intervals of 0.61 m with three observation intervals in O21 every 0.91 m (center to center). A total of 120 head responses (3 periods x 10 tests x 4 intervals) were available for analysis.

Table 1

4. Description and processing of the data set

4.1. Head data

The time and head for each of the 120 head responses was extracted from the raw logger data. Each head recording was referenced to the start time of the corresponding test and normalized relative to the static head prior to the start of the test (e.g., Figure 5). The periodic signal was then corrected to eliminate the influence of incomplete stabilization with the ambient head. This was only observed for a few observation intervals after the packers had been inflated in less permeable material. For these intervals, a linear equation representing the global deviation was fitted to the measurements and then subtracted from them to obtain only the periodic component of the signal (e.g. Fischer et al., 2020). No correction was required for the source intervals. Table 2 summarizes the head recordings extracted for the field experiment. It can be observed that the variation of the head for the source intervals is between 0.126 and 1.386 m (H_0 in Table 2), while the variations for the observation intervals are between 0.001 and 0.0189 m (h_0 min and h_0 max in Table 2). The comparison of the head between the source and the observation intervals indicates a strong attenuation of the head in the aquifer.

Table 2

Figure 5 shows examples of head recordings in the source interval and the three observation intervals for test S18.630 for the three periods. Several observations can be derived from the data. First, while the variation of the displacement of the rod is the same for all periods ($A_0=1.25$ m in Table 1), the variation of the head in the source interval decreases with the length of the period.

The variation for the period of 600 s is less than a quarter of the variation for the period of 150 s. This is explained by the fact that the slower the displacement of the water column in the riser (e.g., period of 600 s), the more water is exchanged with the aquifer and the less is stored in the borehole (Paradis et al. 2024). Second, the variation of the head for the observation intervals is similar for all periods, although the head in the source interval is much larger for the shortest period. This illustrates the concept of attenuation of head in aquifers, which is more significant for shorter periods (e.g., Ferris, 1952). When planning periodic slug tests, wellbore storage and aquifer attenuation must therefore be considered. Finally, it is noted that the head for the intervals O21.690 and O21.600, which are 0.91 m apart as shown in Figure 3, show similarities. However, a comparison of the amplitudes and phase shifts between O21.600 and O21.510, which are also 0.91 m apart, shows clear differences. This indicates strong contrasts in the hydraulic properties between the two pairs of intervals.

Figure 5

To reduce the computation time of the numerical inversions, the original 1 Hz head measurements were subsampled to 15 points per cycle (Figure 6). First, a moving average with window sizes of 10, 20 and 40 s were applied to tests with periods of 150, 300 and 600 s, respectively. The head values in the middle of these time windows were then selected to represent the average head at intervals of 10, 20 or 40 s.

Figure 6

4.2. Noise level

The noise level of the head data was assessed by fitting a sinusoidal curve to the original head measurements (Figure 7). The fit was applied to a complete cycle after the early transient effect had disappeared. The noise level is expressed as the standard deviation of the residual between the sinusoid and the measurements. Figure 7 shows that the noise level in the source interval is higher than in the observation intervals. The noise level also remains constant across the observation intervals, regardless of the variation of the head. For example, the intervals O21.690 and O21.600, which have four times the amplitude of O21.510, have similar standard deviations.

Figure 7

Figure 8 and Table 3 also show that the noise level in the source intervals is larger for the shortest period. This is due to the faster movement of the rod at shorter periods, which causes more turbulent flow in the annular space between the rod and the riser tube (Figure 4b). For the observation intervals, the noise level is similar for all periods and depends only on the precision of the pressure loggers used for the experiment. It is unlikely that the noise generated in the source intervals will be transferred to the observation intervals, as the head in the aquifer is strongly attenuated. The median standard deviation of the noise level for the source intervals is 3.1×10^{-2} , 1.4×10^{-2} , and 8.6×10^{-3} m for the periods of 150, 300, and 600 sec, respectively. For the observation intervals, the noise level ranges from 4.9×10^{-4} to 5.3×10^{-4} m. Although the variation of the head in the observation intervals is small (Table 2), the experiment provided head data with a high signal-to-noise ratio, indicating excellent data quality.

Table 3

Figure 8

4.3. Test redundancy

To validate the reproducibility of the head recordings, redundant tests were incorporated into the experiment (Figure 2 and Table 1). For example, the test S18.510a was performed with O21.510 as the lower observation interval of the packer arrangement in O21. After the packer arrangement in O21 was moved down, test S18.510b was performed with O21.510 as the upper intervals of the arrangement. The same was done for S18.690a-b and O21.690. Figure 9 shows the redundant head recordings, which demonstrate the excellent reproducibility of the tests.

Figure 9

4.4. Calculation of the periodic flow rate

To simulate the periodic tests, the volume of water displaced into the riser tube by the movement of the rod is calculated (Figure 4). The periodic change in the volume of water Q at each time t is calculated using the following formula:

$$Q = \frac{2A_0 r_0^2 \pi^2}{T_0} \cos\left(\frac{2\pi}{T_0} t\right) \quad \text{Equation (1)}$$

where r_o is the radius of the rod, A_o the peak amplitude of the displacement of the rod and T_o the period of the signal. A sinusoidal displacement of the rod is assumed here; therefore Equation 1 is the derivative of the sinusoidal displacement ($A_o \sin\left(\frac{2\pi}{T_o} t\right)$) multiplied by the cross-section of the rod (πr_o^2).

For the simulations, Q is approximated as a series of steps, where each step is modeled as a constant flow boundary condition with a start and end time (Figure 6). The number of steps corresponds to the number of measurements of the subsampled head recordings with a measurement in the middle of each flow rate step.

5. Simulation of the tomography experiments

The numerical inversion of each tomography experiment was performed using a parallelized version of the lr2dinv simulator (Bohling and Butler, 2001) modified by the authors. In the lr2dinv simulator, a forward radial groundwater flow model is coupled with the Levenberg–Marquardt algorithm to simultaneously estimate the spatial distribution of K_h , K_v/K_h , and S_s . The radial groundwater flow equation is solved using a block-centered finite-difference formulation after a logarithmic transformation of the radial flow equation to an equivalent equation in Cartesian coordinates (Butler and McElwee, 1995; Bohling and Butler, 2001). The Levenberg–Marquardt algorithm is a hybrid approach that combines the gradient descent and the Gauss–Newton methods to iteratively solve nonlinear least squares parameter estimation problems (Marquardt, 1963; Press et al., 1992). A series of four simulations were run, with three independent inversions for each of the periods and a fourth combining data from the three periods (Table 4). The same model structure was used for all simulations. The next sections describe the development of the numerical model applied to the inversion of the experiment data.

Table 4

5.1. Simulation and parameter grids

All inversions used a simulation grid consisting of 43 cells with an exponentially increasing width along the radial axis and 34 cells with a constant height of 0.30 m along the vertical axis (Figure 10a). The width of radial cells is smaller near the source well to better simulate the higher hydraulic gradients in this zone. The simulation grid was designed to match the locations of the packers and screens used for the field experiment. Thus, the packers and source intervals vertically comprise two simulation cells, while the observation intervals are represented by a single cell. The observation well, 5.35 m from the source well, is also placed directly on the nodes of the simulation grid.

The simulation grid is overlaid with a parameter grid including 13 layers (numbered L1 to L13 in Figure 10a) and 8 columns (C1 to C8). Layers L2 to L12 have a thickness of 0.61 m to correspond to the length of the source intervals, while the layers above and below the tested zone were made thicker. Along the horizontal, the parameter grid consists of seven columns between the source and observation wells (C1 to C7), with an average width of 1.0 m. The width of columns is variable to adapt them to the simulation grid, which has an exponentially increasing size. A larger column of 54.85 m width is used beyond the observation well to average the influence of the hydraulic properties outside the tested zone. The same discretization of the parameter grid is used for K_h , K_v/K_h , and S_s .

Figure 10

5.2. Boundary and wellbore conditions

To accurately simulate the variation of the head measured by the logger located in the screen of the source intervals (“fixed logger” in Figure 4a), the annular space between the rod and the riser tube is converted to a corresponding radius. The equivalent radius r_{eq} is obtained using the following formula:

$$r_{eq} = \sqrt{(r_i^2 - r_o^2)} \quad \text{Equation (2)}$$

where r_i and r_o are the radii of the riser and the rod respectively (Figure 3b). The value of r_{eq} used by the simulator was 0.00772 m.

The outer boundary of the model, represented by a fixed head, was placed 49.5 m from the source well to avoid interference during the simulated tests (Figure 10a). The upper boundary is also a fixed head to approximate the position of the water table of the unconfined aquifer, which did not fluctuate significantly in response to the tests. The impermeable lower boundary has a zero-flux condition. The simulation of the effects of wellbore storage and packer placement in the source well is approximated using a formulation of Darcy's Law (Bohling and Butler, 2001), with the screen of the source interval modeled as a region of high permeability and the packers as essentially impermeable (Figure 10b). With this option, a column of model cells is used to represent the region inside the wellbore from the radius of the well, r_w , to the inner radius of the model grid ($< r_w$), with Q from Equation 1 placed at the inner radius. Thus, the water balance resulting from the flow rate Q induced by the movement of the rod is the sum of the flow represented by the change in storage related to the change in water level in the well Q_w and the flow exchanged with the aquifer Q_a :

$$Q = Q_w + Q_a = \pi r_{eq}^2 \frac{\partial h}{\partial t} + 2\pi r_w L K_h \frac{\partial h}{\partial r} \quad \text{Equation (3)}$$

where $\frac{\partial h}{\partial t}$ is the change in water level in the source interval, L is the length of the source interval, and $\frac{\partial h}{\partial r}$ is the radial hydraulic gradient at the interface between the screen and the aquifer. Wellbore properties are given separately for each test to account for the repositioning of the double packer arrangement in the source well. Note that without the wellbore option, Q_a must be used instead of Q because the amplitude of head and lag of responses in the simulated aquifer may not accurately represent field measurements. This exchange flow rate Q_a can be estimated using equation 3 (e.g. equation 1 in Cheng and Renner, 2018). Wellbore storage in the observation intervals was neglected as packers were isolating the screens (Sageev, 1986). The average head of the nodes that coincide with the observation intervals represents the head in these intervals (Figure 10c).

5.3. Inversion strategy

The strategy for inversion of heads from the tomography experiments involved first creating an initial model of hydraulic parameters \mathbf{p} of the aquifer with preliminary estimates for K_h , K_v/K_h , and S_s . The initial model for each heterogeneous simulation (simulations b in Table 4) was obtained from the inversion of a homogeneous model using all tests associated with the simulation (simulations a in Table 4). These initial models with different values of K_h , K_v/K_h , and S_s for each model represent the “effective hydraulic properties” of the aquifer. This strategy facilitated the search for the optimal solutions. The groundwater flow simulator was then used to perform a forward simulation to predict the head based on the initial model, and the residuals between the measured heads h_i and the heads predicted by the simulation $f_i(\mathbf{p})$ were calculated.

The Levenberg-Marquardt algorithm was then used to iteratively adjust the hydraulic parameters to minimize the residuals according to the following chi-squared objective function:

$$\chi^2 = \sum_{i=1}^n \left(\frac{h_i - f_i(\mathbf{p})}{\sigma_i} \right)^2 \quad \text{Equation (4)}$$

where σ_i is a scaling factor associated with each measurement. Scaling factors were used to weigh the objective function according to the relative magnitude in head for the source and observation intervals. This is necessary for fitting equally well the heads of the observation intervals, which are up to three orders of magnitude lower than the heads in the source intervals (Table 2). The scaling factors were determined by comparing the average variation of the head measured in the source and observation intervals (H_0 and h_0 max in Table 2). The same global scaling factors of 0.52 for source intervals and 0.0068 for observation intervals were used for all inversions. The minimization

of the objective function was achieved using an implicit row-oriented directional line iteration method.

At each iteration, the sensitivity matrix \mathbf{J} of the residuals with respect to the hydraulic parameters estimated at the current iteration was first calculated. The sensitivity matrix is an i -by- j normalized sensitivity matrix of i measurements and j hydraulic parameters, expressing the head response at each observation point and at each time to a change in each hydraulic parameter value:

$$J_{i,j} = \frac{1}{\sigma_i} \frac{\partial(h_i - f_i(\mathbf{p}))}{\partial p_j} / \hat{p}_j \quad \text{Equation (5)}$$

where \hat{p}_j represents the estimated value of the j^{th} hydraulic parameter. This normalized form of the sensitivities is used to better identify the relative influence of each hydraulic parameter. The elements of the sensitivity matrix were evaluated using the sequential perturbation approach of a groundwater flow model developed with the lr2dinv simulator.

The hydraulic parameters were then updated at each iteration k using the Levenberg-Marquardt rule:

$$\mathbf{p}_{k+1} = \mathbf{p}_k - (\mathbf{J}^T \mathbf{J} + \lambda \mathbf{I})^{-1} \mathbf{J}^T \mathbf{r} \quad \text{Equation (6)}$$

where \mathbf{r} is the vector of scaled residuals $\frac{h_i - f_i(\mathbf{p})}{\sigma_i}$ and λ is the damping factor that controls the interpolation between the gradient descent and Gauss-Newton methods. The algorithm dynamically adjusts λ to ensure a slow but stable solution when the hydraulic parameters are far from the optimal solution and faster convergence as they approach the optimal solution. This iterative process continued until convergence criteria were met that is a chi-squared error $< 1 \times 10^{-8}$ or a change in hydraulic parameter values $< 1 \times 10^{-3}$.

For each inversion listed in Table 4, all tests and intervals were processed simultaneously for the corresponding source signal period. The static initial condition before each test was simulated with a constant head of 0 m for the entire simulation grid, representing the relative head (change) from to the initial conditions. No model regularization was used in the minimization of the objective function, so that only the information contained in the measured heads is used to estimate the hydraulic properties.

6. Results and discussion

6.1. Analysis of the residuals

Table 5 summarizes the statistics of the residuals between observed and predicted head for the four inversion scenarios listed in Table 4. As observed in the analysis of the noise level, the standard deviation of the residuals for the source intervals is larger than for the observation intervals and decreases with the period. In the simulation that combines the three periods, the standard deviation is close to the average of the individual simulations. The standard deviation for the observation intervals increases slightly with the period, whereby the value for the combined simulation is the highest. Overall, the standard deviation of the residuals is very small, considering that it is only 1.5 to 1.7 times the noise level estimated for the observation intervals (subsampling head data in Table 3) and 2.1 to 3.6 times for the source intervals. This difference is the result of cumulative errors or simplifications related to the field operations, data processing, model construction or numerical analysis.

Table 5

Figure 11a provides additional insight into the effectiveness of the inversion process and shows a strong agreement between the measured and simulated head for the tomography experiment with a period of 300 s (Simulation 2b in Table 4). The amplitude and phase of the simulated head responses are also generally in very good agreement with the measurements (Figure 12). The coefficient of determination and the slope of the linear regression are above 0.96 for all tomography experiments (Table 5).

In addition, Figures 11a and 11c illustrate the discrepancy in the quality of agreement that can be obtained relative to observations between a heterogeneous and a homogeneous model and thus emphasize the necessity to consider the heterogeneity of the test site to reproduce observations. The importance of using a model explicitly considering anisotropy can also be seen when comparing Figures 11a and 11b. As shown in Figure 2, isotropic conditions cannot be assumed for measurement having a vertical resolution of 0.15 m, and the range of anisotropy is quite variable. An anisotropic model can therefore better capture the effects of smaller scale heterogeneity on the heads. Figure 13 also shows that the contrast in K_h and S_s is stronger in the heterogeneous and isotropic model (Figure 13b) than in the heterogeneous and anisotropic model (Figure 13a) to compensate for the simplified hydrogeology of an isotropic model. Of course, the cells of the parameter grid could be reduced to a size at which isotropic conditions could be assumed. However, centimetric cell sizes would probably have been necessary for the study area, which would have led to an unacceptable computational effort given the enormous increase in the number of cells.

In summary, the analysis of the residuals shows that the inversion process accurately captured the general behavior of head responses influenced by heterogeneity. This is also remarkable considering the short simulation runtimes of about one and a half hours for the individual simulations (Table 5).

Figure 11

Figure 12

Figure 13

6.2. Profiles of hydraulic properties

Figure 14 shows the profiles of the hydraulic properties estimated by inversion along the source and observation wells for the four heterogeneous models listed in Table 4. Overall, the K_h and K_v/K_h profiles are similar for all simulations, with only a few intervals within the focus area showing significant deviations. The S_s profiles along the observation well also show similar trends for the individual periods but differ more significantly at the source well.

Figure 14

The ratio of H_0/A_{eq} in Table 2 is also plotted in Figure 14a for comparison. H_0 is the variation of the head measured in the source interval, while A_{eq} is calculated using the following equation:

$$A_{eq} = \frac{A_0 r_o^2}{r_{eq}^2} \quad \text{Equation (7)}$$

A_{eq} thus represents the maximum variation of the head that could be achieved in the source interval for a given value of A_0 and with the specific radii r_o and r_{eq} of the experimental setup if there were no water exchange with the aquifer. A ratio of H_0/A_{eq} equal to 1 means that there is no water exchange between the well and the aquifer, while a ratio of 0 means all water flows into the aquifer. Figure 14a shows that the patterns of H_0/A_{eq} values (with inverted scale) and K_h are similar, but with different magnitudes of the ratios depending on the period of the source signal. This illustrates

the control that K_h and the signal period exert on the volume of water that can be exchanged between the well and the aquifer.

Figure 14 also shows a limited agreement between the profiles of hydraulic properties and the grain size indications provided by cone penetrometer soundings. Although one might expect the maximum K_h values to occur in the interval where sand units (yellow) are prominent, the higher values are somewhat offset. Such high K_h values are found at the bottom of the thicker sand unit along S18 (about 111 m elevation) and at the bottom of the focus area for O21 (about 110 m), where a mixture of silt and sand is observed. However, the higher K_h values do correspond to intervals where coarser sand predominates. For K_v/K_h , greater anisotropy would have been expected where the silt and sand units alternate (e.g., in the lower part of the focus area). However, the general trend for the two profiles is that stronger anisotropy ($\sim 1 \times 10^{-2}$) is found in the upper half of the focus area, whereas more isotropic conditions ($> 1 \times 10^{-1}$) are present in the lower half. The isotropic conditions are also found where K_h is higher, which may indicate that sediments deposited under higher energy are less stratified. For S_s , the correlation with geology is more difficult to define. This parameter is primarily influenced by the compressibility of the aquifer matrix and the history of stress changes in the aquifer or during sediment deposition, making it difficult to link directly to the sediment characteristics alone.

This comparison of indicators of sediment size with hydraulic properties illustrates the difficulties often encountered when attempting to quantify hydraulic properties based on geological descriptions of materials. For example, sediments at the study site in the same lithologic units (based on mean sediment grain size) may have differences in K_h and K_v values of up to two orders of magnitude (Paradis *et al.*, 2014). Variations in sediment sorting (from moderately well sorted to very poorly sorted) associated with the littoral depositional environment, which is not fully captured by the mean grain size, explain these variations in permeability for apparently similar sediments. This illustrates the importance of favoring direct estimates of hydraulic properties with hydraulic tests over indirect estimates based on proxies to effectively capture the specific conditions of a site.

6.3. Tomograms of hydraulic properties

Figure 15 shows the tomograms for K_h , K_v/K_h , and S_s obtained from the inversion of the periodic test data from the three individual periods and the combination of data from the three periods. Like the profiles, the tomograms for K_h and K_v/K_h show similar general spatial distributions for the four inversions, but they differ slightly for S_s . The tomograms for K_h show that the lower part of the focus area is crossed by a layer with higher K_h . Similarly, the tomograms for K_v/K_h show a region of moderate to high anisotropy in the middle of the focus area. The tomograms for S_s are similar in the upper part of the focus area, whereas they differ significantly in the lower part.

Figure 15

These similarities are also apparent in the statistics of hydraulic properties (Figure 16). Despite a slight decrease in K_h and a slight increase in K_v/K_h and S_s with period, the median values for each hydraulic property are close for all inversions. The median values for the inversion combining the three periods are intermediate between the values obtained for each individual period. The variability of the hydraulic property values, indicated by the range of 25-75% quantiles, decreases with period for K_h and K_v/K_h . With S_s , the variability is more constant but increases slightly for the period of 600 s. The variability for the combined inversion is also between the values for each period. Note that the increase in variability could be the result of better spatial resolution of the heterogeneity or uncertainties in the estimates due to the lack of information in the heads to constrain the inversion.

Figure 16

6.4. Cross-verification

Since the real hydraulic properties of an aquifer are not known in field-based studies, it is not possible to directly assess the accuracy of a hydraulic property model by comparing it with reality. However, differences in information content between models can be assessed by comparing their performance in predicting heads using independent hydraulic tests that were not included in the original analysis to produce these models. Models that predict heads equally well from independent tests are assumed to have similar hydraulic properties. In this section, we propose a cross-verification procedure in which each of the three inverted models from one period is used to simulate the heads from another period to evaluate the differences in information content (e.g., the projection of the tests with a period of 150 s to the tomograms obtained from the inversion using the tests with the period of 300 s). The model that combines the three periods is also tested with the three periods individually. A total of nine scenarios are simulated (Table 6). This procedure is performed with the numerical model in forward mode.

Figure 17 shows the results of the cross-verification procedure for the six scenarios with individual periods. First, it is noticeable that the standard deviation of the projected simulations is consistently greater than that of the original inversions for the same period. This discrepancy indicates that the different periods convey different information about the hydraulic properties. Only identical fields or periodic tests with the same sensitivity to the hydraulic properties would have yielded the same residuals (or very specific combinations of hydraulic property fields contingent on highly specific circumstances or field configurations). This becomes even clearer when comparing the differences in the standard deviation, which are greatest for the two extreme periods (150 s and 600 s). The smallest differences are found in the models that were inverted with the periods of 300 s and 600 s. A similar interpretation was obtained by Fischer et al. (2018) for cross-verification with two periodic signals in a karst aquifer.

Table 6 also shows the performance statistics for the scenarios with the combined model. As with the inversions with the single period, the standard deviations of the residuals for the three periods with the combined model are higher than for the original combined inversion. But the differences in the standard deviations are similar for the three periods. This indicates that the combined inversion finds the best compromise to reproduce the head responses of the tests with different periods. These similarities in the differences in the residuals are to be expected since the tests used for the projection with the combined model are not truly independent, as each scenario has the same period as one of the three periods used in the combined inversion. Table 6 also shows that the differences in the standard deviations with the combined model are smaller than in the inversions with the single period. This indicates that the combined model is a better "effective model" of the hydraulic properties to reproduce the general flow conditions for the range of aquifer stimulation used in this study.

Figure 17

Table 6

6.5. Verification with conventional slug tests

To further evaluate the difference in the information content of the models of hydraulic properties obtained from the inversion of periodic slug tests, conventional slug tests were simulated in forward mode with the four inverted models obtained from single and combined periods. The conventional slug tests were performed in a tomographic arrangement at the same source and observation intervals used for the periodic tests. Six tests were available for the intervals S18.510a to S18.750 (see Figure 3 for the location of the intervals). Figure 18 shows an example of the good agreement between the measured head and the simulated head for an example related to the inverted parameter field obtained from the tomographic experiment with a period of 300 s. Both the amplitude and the time delay of the maximum head of the response for the observation intervals are generally well reproduced. Table 7 describes the statistics of the residuals for the verification simulations, and shows that the standard deviation of the scaled residuals for the simulation with a period of 300 s is the smallest. This result is unexpected, as the 150 s period was anticipated to perform better due to its greater similarity to the stresses induced in the aquifer by the slug tests, compared to the longer periods. However, the higher noise level associated with the 150 s period may have reduced the resolution of the hydraulic properties, potentially explaining these findings (Figure 8). As for the cross-verification, the difference in the standard deviation is similar for the periods of 300 s and 600 s and quite different for the period of 150 s. Additionally, the fit for the model with the combination of the three periods lies between those of the experiments with a single period.

Table 7**Figure 18**

7. Conclusions

This study presented a complete example of the practical application of hydraulic tomography with periodic tests to a littoral aquifer, covering field procedures, data processing and data inversion. The periodic signals of the tomographic tests were obtained mechanically with a rod attached to a computer-controlled winch. This system allowed the generation of a sinusoidal displacement of the rod with adjustable amplitude and period. The field experiment involved 30 periodic tests performed in small intervals isolated by packers in two fully screened wells. Three different periods were used, and for each period a total of 40 head responses were measured in the source interval and in three intervals of an adjacent observation well. The head records were analyzed by numerical inversion to estimate the 2D distribution of hydraulic properties between the two test wells. Inversion was performed by simulating the radial groundwater flow equation in combination with the Levenberg-Marquardt algorithm. The analysis considered K_h , K_v/K_h , and S_s , as well as wellbore storage in the source well. Periodic tests were inverted individually for each period and for the combination of data from all tests. To the author's knowledge, these are the first tomography experiments with periodic signals that consider the anisotropy of hydraulic conductivity.

The key findings from this field proof-of-concept of periodic slug tests conducted in a tomography configuration between wells are manifold:

Testing devices and procedures. This study shows that the field experiment yielded high quality head measurements despite the challenges of conducting tests at small intervals in a heterogeneous environment where anisotropy strongly attenuates the signal in observation intervals. The experimental setup, with a small equivalent radius (r_{eq}), significantly enhanced signal quality by enabling substantial water level fluctuations in the source intervals (A_{eq}) for the given volume of water displaced by the rod (A_0), effectively acting as an “amplifier” for the head (e.g. $A_{eq} > A_0$). However, the limited volume of water used in each test restricted the experiment to a narrow range of periods. Shorter or longer periods than those reported in this study resulted in lower heads, which were within the noise level. In addition, the rod length used for the tests could not be increased further due to the shallow water table, which limited the amplitude of the generated signal. These limitations highlight the need for developing new testing equipment and procedures that are versatile and capable of generating broader range of periods and higher-amplitude signals. The pneumatic source described by Sayler et al. (2018) shows promise for generating a broader range of periods and offers the advantage of no net removal of water at the surface, which is beneficial for sites where water disposal or mobilization of pollutants could be a concern.

Anisotropy of hydraulic conductivity. Furthermore, this study shows that the anisotropy of hydraulic conductivity (K_v/K_h) can be effectively estimated using tomography experiments with periodic tests. The results agree well with the values of previous studies at the test site. The estimation of K_v/K_h is enabled by the small aspect ratio of the source interval (length of the screen to the radius of the screen), which promotes significant vertical flow in the aquifer (Paradis and Lefebvre, 2013). The comparison of the isotropic and anisotropic scenarios for the analysis of the hydraulic tests has also shown the importance of K_v/K_h . However, it is important to note that the heterogeneities reflected for given degree of anisotropy are often scale-dependent. Variations in experimental setups (e.g., different lengths of source intervals) and numerical configurations (e.g., different discretization of model cells) can lead to different estimates of K_v/K_h . While experimental and model scales can be refined to better capture the heterogeneous nature of aquifers, no type of field evidence can definitively confirm whether a particular discretization is fine enough to assume isotropic conditions. Regardless of the discretization chosen, the use of an anisotropic framework for tomographic data analysis increases confidence in the estimated model parameters. Even if the analysis ultimately shows that anisotropy is unnecessary, an isotropic model derived from an anisotropic approach is inherently more robust and reliable; an approach widely accepted for decades in the geophysics community (Babuska and Cara, 1991). The inclusion of K_v/K_h in numerical models then has the potential to significantly improve the accuracy of groundwater flow simulations (Shepley, 2024) and optimize the effectiveness of pump-and-treat systems for contaminant recovery (Bair and Lahm, 1996). Future research should investigate the effects of varying experimental scales and discretization levels on the estimation of anisotropy and examine how these factors influence groundwater flow models and contaminant recovery systems at different scales. Additionally, expanding these findings to other aquifer types with varying degrees of heterogeneity and anisotropy could provide valuable examples from diverse geological environments. This broader understanding of the hydraulic property characteristics of various settings would enhance knowledge and help guide best practices in hydrogeological applications.

Information content of the periods. Finally, the results of this study show that the inversion of individual periods or their combination leads to slightly different models of hydraulic properties, indicating that they convey similar information. These differences are reflected in the spatial and statistical distribution of the hydraulic properties and in the ability of each model to reproduce the heads obtained from independent periodic and conventional slug tests. The relatively narrow range of periods used in this study (150, 300 and 600 s) may explain the small differences in the estimated hydraulic properties, as each period could have examined similar spatial scales within the aquifer. However, the difference in information content is more pronounced for the extreme periods (150 and 600 s), supporting the idea that contrasting periods may carry complementary information (e.g., Rosa and Horne, 1997). Although this is not explicitly demonstrated in this field study, shorter periods could provide more detailed insights into near-field hydraulic responses, while longer periods might capture broader, integrated properties over larger distances (e.g., Ahn and Horne, 2010; Paradis et al., 2024). Although the combined inversion integrated data from multiple periods, the verification with conventional slug tests performed no better than the average of the inversions for individual periods. This is in line with the theoretical analysis proposed by Wang et al. (2021), which suggests that “multifrequency tests do not increase the resolution of aquifer characterization”

because “the sensitivity maps of different frequencies are highly correlated.” However, tomography experiments with a wider range of periods could have led to a different conclusion. As shown by Paradis et al. (2024) with synthetic aquifers, the choice of the period is crucial for aquifer resolution. Short periods with significant transient responses, as well as large differences in period lengths (both shorter and longer than those used in this field study), could help reduce the sensitivities of the head to the hydraulic parameters and improve resolution. Future work should prioritize experimenting with a broader range of periods to evaluate how variations, particularly extreme period lengths, affect the resolution and sensitivity of aquifer characterization. These experimental efforts should be complemented by fundamental studies that quantitatively assess the information content of the experiments, providing a stronger theoretical foundation for optimizing and interpreting hydraulic tomography applications.

Acknowledgment

Sincere thanks are extended to F. Huchet and V. Boisvert for their precious contribution during the field investigation. B. Giroux is acknowledged for the parallelization of the simulator *lr2dinv*. N. Benoit is also thanked for the internal review of the paper. The device brands mentioned in this work are for information purposes only, to document procedures, and do not constitute a recommendation for these specific products. This is a GSC contribution 20230267.

References

- Ahn, S., Horne, R.N., 2010. Estimating permeability distributions from pressure pulse testing. In Proceedings - SPE Annual Technical Conference and Exhibition, 3:2388–2403. Florence, 10.2118/134391-MS
- Babuska, V. and M. Cara (1991) Seismic Anisotropy in the Earth. Kluwer Academic Publishers, Boston, 227 pp.
- Bair, E.S., Lahm, T.D., 1996. Variations in capture-zone geometry of a partially penetrating pumping well in an unconfined aquifer. *Groundwater*, 34: 842-852. <https://doi.org/10.1111/j.1745-6584.1996.tb02079.x>
- Barry, F., Ophori, D., Hoffman, J., Canace, R., 2009. Groundwater flow and capture zone analysis of the Central Passaic River Basin, New Jersey. *Environmental Geology* 56, 1593–1603.
- Becker, M.W., Gultinan, E., 2010. Cross-hole periodic hydraulic testing of inter-well connectivity. In: Thirty-Fifth Workshop on Geothermal Reservoir Engineering. Stanford University, Stanford, California
- Berg, S.J., Illman, W.A., 2015. Comparison of hydraulic tomography with traditional methods at a highly heterogeneous site. *Groundwater* 53 (1), 71-89. doi:10.1111/gwat.12159.
- Berg, S.J., Illman, W.A., 2011. Three-dimensional transient hydraulic tomography in a highly heterogeneous glaciofluvial aquifer-aquitard system. *Water Resour. Res.* 47, W10507. doi:10.1029/2011WR010616.

- Black, J.H., Kipp, K.L.J., 1981. Determination of hydrogeological parameters using sinusoidal pressure tests: A theoretical appraisal. *Water Resour. Res.* 17 (3), 686–692. doi:10.1029/WR017i003p00686.
- Boggs, J.M., Young, S.C., Beard, L.M., 1992. Field study of dispersion in a heterogeneous aquifer 1: Overview and site description. *Water Resour. Res.* 28 (12), 3281–3291.
- Bohling, G.C., 1993. Hydraulic tomography in two-dimensional, steady-state groundwater flow. *Eos Trans. AGU* 74, 141.
- Bohling, G.C., Butler, J.J., 2001. lr2dinv: A finite-difference model for inverse analysis of two-dimensional linear or radial groundwater flow. *Comput. Geosci.* 27, 1147–1156. doi.org/10.1016/S0098-3004(01)00036-X
- Bohling, G.C., Butler, Jr.J.J., Zhan, X., Knoll, M.D., 2007. A field assessment of the value of steady shape hydraulic tomography for characterization of aquifer heterogeneities. *Water Resour. Res.* 43, W05430. doi:10.1029/2006WR004932.
- Bolduc, A., 2003. Géologie des formations superficielles, Charny, Québec. Commission Géologique du Canada, Dossier public 1976, échelle 1/50000, Ottawa, Canada.
- Brauchler, R., Hu, R., Dietrich, P., Sauter, M., 2011. A field assessment of high-resolution aquifer characterization based on hydraulic travel time and hydraulic attenuation tomography. *Water Resour. Res.* 47, W03503. <http://dx.doi.org/10.1029/2010WR009635>.
- Brauchler, R., Hu, R., Hu, L., Jimenez, S., Bayer, P., Dietrich, P., Ptak, T., 2013. Rapid field application of hydraulic tomography for resolving aquifer heterogeneity in unconsolidated sediments. *Water Resour. Res.* 49 (4), 2013–2024.
- Butler Jr., J.J., McElwee, C.D., 1995. Well-testing methodologies for characterizing heterogeneities in alluvial-aquifer systems: final technical report. Kansas Geological Survey Open File Report 95-75.
- Butler, Jr.J.J., Dietrich, P., Wittig, V., Christy, T., 2007. Characterizing hydraulic conductivity with the direct-push permeameter. *Ground Water* 45 (4), 409–419.
- Cardiff, M., Zhou, Y., Barrash, W., Kitanidis, P.K., 2020. Aquifer imaging with oscillatory hydraulic tomography: Application at the field scale. *Groundwater* 58 (5), 710–722. doi:10.1111/gwat.12960.
- Cardiff, M., Bakhos, T., Kitanidis, P.K., Barrash, W., 2013. Aquifer heterogeneity characterization with oscillatory pumping: Sensitivity analysis and imaging potential. *Water Resour. Res.* 49 (9), 5395–5410. doi.org/10.1002/wrcr.20356.
- Cardiff, M., Barrash, W., Kitanidis, P.K., Malama, B., Revil, A., Straface, S., Rizzo, E., 2009. A potential-based inversion of unconfined steady state hydraulic tomography. *Ground Water* 47 (2), 259–270.

- Cheng, Y., Renner, J., 2018. Exploratory use of periodic pumping tests for hydraulic characterization of faults. *Geophys. J. Int.* 212 (1), 543–565, [10.1093/gji/ggx390](https://doi.org/10.1093/gji/ggx390)
- Crisman, S.A., Molz, F.J., Dunn, D.L., Sappington, F.C., 2001. Application procedures for the electromagnetic borehole flowmeter in shallow unconfined aquifers. *Ground Water Monit. R.* 21 (4), 96-100.
- de Marsily, G., Delay, F., Gonçavès, J., Renard, P., Teles, V., Violette, S., 2005. Dealing with spatial heterogeneity. *Hydrogeol. J.* 13, 161–183.
- Dubreuil-Boisclair, C., Gloaguen, E., Marcotte, D., Giroux, B., 2011. Heterogeneous aquifer characterization from ground-penetrating radar tomography and borehole hydrogeophysical data using nonlinear Bayesian simulations. *Geophysics* 76 (4), 1–13. doi.org/10.1190/1.3571273
- Falta, R.W., Basu, N., Rao, P.S., 2005. Assessing impacts of partial mass depletion in DNAPL source zones: II. Coupling sources strength functions to plume evolution. *Journal of Contaminant Hydrology* 79, 45–66.
- Ferris, J.G., 1952. Cyclic fluctuations of water level as a basis for determining aquifer transmissibility. United States Geological Survey, Washington, D.C. 16 pp. doi.org/10.3133/70133368
- Fischer P., Jardani, A., Jourde, H., Cardiff, M., Wang, X., Chedeville, S., Lecoq, N., 2018. Harmonic pumping tomography applied to image the hydraulic properties and interpret the connectivity of a karstic and fractured aquifer (Lez aquifer, France). *Adv. Water Resour.* 119, 227-244. <https://doi.org/10.1016/j.advwatres.2018.07.002>
- Fischer, P., De Clercq, T., Jardani, A., Massei, N., Abbas, M., 2020. Imaging the hydraulic properties of a contaminated alluvial aquifer perturbed with periodic signals. *Hydrogeol. J.* 28, 2713–2726. doi.org/10.1007/s10040-020-02233-8
- Frei, S., Fleckenstein, J.H., Kollet, S.J., Maxwell, R.M., 2009. Patterns and dynamics of river–aquifer exchange with variably-saturated flow using a fully-coupled model. *J. Hydrol.* 375, 383-393. doi.org/10.1016/j.jhydrol.2009.06.038
- Gernez S., Bouchedda, A., Gloaguen, E., Paradis, D., 2019. Comparison between hydraulic conductivity anisotropy and electrical resistivity anisotropy from tomography inverse modeling. *Front. Environ. Sci.* 7, 67. doi: 10.3389/fenvs.2019.00067
- Gloaguen, E., Lefebvre, R., Ballard, J.M., Paradis, D., Tremblay, L., Michaud, Y., 2012. Inference of the two-dimensional GPR velocity field using collocated cokriging of direct push permittivity and conductivity logs and GPR profiles. *J. Appl. Geophys.* 78, 94-101. doi.org/10.1016/j.jappgeo.2011.10.015
- Gottlieb, J., Dietrich, P., 1995. Identification of the permeability distribution in soil by hydraulic tomography. *Inverse Probl.* 11, 353–360. <http://dx.doi.org/10.1088/0266-5611/11/2/005>.

- Gultinan, E., Becker, M.W., 2015. Measuring well hydraulic connectivity in fractured bedrock using periodic slug tests. *J. Hydrol.* 521, 100-107. [10.1016/j.jhydrol.2014.11.066](https://doi.org/10.1016/j.jhydrol.2014.11.066)
- Hanson, R.T., Nishikawa, T., 1996. Combined use of flowmeter and time-drawdown data to estimate hydraulic conductivities in layered aquifer systems. *Ground Water* 34 (1), 84-94.
- Hart, D.J., Bradbury, K.R., Feinstein, D.T., 2006. The vertical hydraulic conductivity of an aquitard at two spatial scales. *Ground Water* 44 (2), 201–211.
- Hochstetler, D.L., Barrash, W., Leven, C., Cardiff, M., Chidichimo, F., Kitanidis, P.K., 2016. Hydraulic Tomography: Continuity and Discontinuity of High-K and Low-K Zones. *Groundwater* 54, 171-185. <https://doi.org/10.1111/gwat.12344>
- Hoque, M.A., Burgess, W.G., 2020. Representing heterogeneity of fluvio-deltaic aquifers in models of groundwater flow and solute transport: A multi-model investigation in the Bengal Basin. *J. Hydrol.* 590, 125507. doi.org/10.1016/j.jhy
- Hommersen, J.D., Quinn, P.M., Parker, B.L., 2021. Evaluating friction and inertial losses from slug tests conducted in a multilevel system. *Water Resour. Res.* 57, e2021WR029794. doi.org/10.1029/2021WR029794
- Illman, W. A., Liu, X., Takeuchi, S., Yeh, T. J., Ando, K., Saegusa, H., 2009. Hydraulic tomography in fractured granite: Mizunami Underground Research site, Japan. *Water Resour. Res.* 45, W01406. [doi:10.1029/2007WR006715](https://doi.org/10.1029/2007WR006715).
- Keller, C.E., Cherry, J.A., Parker, B.L., 2014. New method for continuous transmissivity profiling in fractured rock. *Groundwater* 52 (3), 352–367.
- Kruseman, G.P., de Ridder, N.A., 2000. *Analysis and Evaluation of Pumping Test Data*. 2nd Edition, International Institute for Land Reclamation and Improvement, 372.
- Lancaster-Jones, P.F.F., 1975. The interpretation of the Lugeon water-test. *Q. J. Eng. Geol.* Vol. 8 (2), 151-154.
- Lavenue, M., de Marsily, G., 2001. Three-dimensional interference test interpretation in a fractured aquifer using the Pilot Point Inverse Method. *Water Resour. Res.* 37 (11), 2659–2675. <https://doi.org/10.1029/2000WR000289>.
- LeBlanc, D.R., Garabedian, S.P., Hess, K.M., Gelhar, L.W., Quadri, R.D., Stollenwerk, K.G., Wood, W.W., 1991. Large-scale natural gradient tracer test in sand and gravel, Cape Cod, Massachusetts, 1: Experimental design and observed tracer movement. *Water Resour. Res.* 27, 895-910.
- Li, W., Englert, A., Cirpka, O. A., Vereecken, H., 2008. Three-dimensional geostatistical inversion of flowmeter and pumping test data. *Ground Water* 46 (2), 193-201.

- Liu, Q., Hu, L., Hu, R., Brauchler, R., Xing, Y., Qi, J., Ptak, T., 2023. Characterization of aquifer heterogeneity by tomographic slug test responses considering wellbore effects. *J. Hydrol.* 627, 130472. doi:10.1016/j.jhydrol.2023.130472
- Liu, G., Butler Jr. J. J., Bohling, G.C., Reboulet, E., Knobbe, S., Hyndman, D.W., 2009. A new method for high-resolution characterization of hydraulic conductivity. *Water Resour. Res.* 45, W08202. doi:10.1029/2009WR008319
- Lochbühler, T., Doetsch, J., Brauchler, R., Linde, N., 2013. Structure-coupled joint inversion of geophysical and hydrological data. *Geophysics* 78 (3), ID1–ID14. doi:10.1190/GEO2012--0460.1.
- Marquardt, D.W., 1963. An algorithm for least squares estimation of nonlinear parameters. *Journal of the Society for Industrial and Applied Mathematics* 11, 431–441.
- Molz, F.J., Morin, R.H., Hess, A.E., Melville, J.G., Guven, O., 1989. The impeller meter for measuring aquifer permeability variations - evaluation and comparison with other tests. *Water Resour. Res.* 25 (7), 1677-1683.
- Morin, R.H., Hess, A.E., Paillet, F.L., 1988. Determining the distribution of hydraulic conductivity in a fractured limestone aquifer by simultaneous injection and geophysical logging. *Ground Water* 2 (6), 587-595.
- Paillet, F.L., 1998. Flow modeling and permeability estimation using borehole flow logs in heterogeneous fractured formations. *Water Resour. Res.* 34 (5), 997-1010.
- Paradis, D., Lefebvre, R., Morin, R.H., Gloaguen, E., 2011. Permeability profiles in granular aquifers using flowmeters in direct-push wells. *Ground Water* 49, 534–547. doi:10.1111/j.1745-6584.2010.00761.x.
- Paradis, D., Lefebvre, R., 2013. Single-well interference slug tests to assess the vertical hydraulic conductivity of unconsolidated aquifers. *J. Hydrol.* 478 (25), 102–118. doi:10.1016/j.jhydrol.2012.11.047.
- Paradis, D., Tremblay, L., Lefebvre, R., Gloaguen, E., Rivera, A., Parent, M., Ballard, J.-M., Michaud, Y., Brunet, P., 2014. Field characterization and data integration to define the hydraulic heterogeneity of a shallow granular aquifer at a sub-watershed scale. *Environ. Earth Sci.* 72, 1325-1348. doi.org/10.1007/s12665-014-3318-2
- Paradis, D., Lefebvre, R., Gloaguen, E., Rivera, A., 2015. Predicting hydrofacies and hydraulic conductivity from direct-push data using a data-driven relevance vector machine approach: Motivations, algorithms, and application. *Water Resour. Res.* 51, 481-505. doi.org/10.1002/2014WR015452
- Paradis, D., Gloaguen, E., Lefebvre, R., Giroux, B., 2016. A field proof-of-concept of tomographic slug tests in an anisotropic littoral aquifer. *J. Hydrol.* 536, 61-73. doi.org/10.1016/j.jhydrol.2016.02.041

- Paradis, D., Lefebvre, Nefzi, A., 2024. Parameter resolution of simulated responses to periodic hydraulic tomography signals in aquifers. *Adv. Water Resour.* 190, 104734. doi.org/10.1016/j.advwatres.2024.104734.
- Parent, M., Occhietti, S., 1988. Late Wisconsinan Deglaciation and Champlain Sea Invasion in the St. Lawrence Valley, Québec. *Geogr. Phys. Quatern.* 42, 215. doi.org/10.7202/032734ar
- Press, W.H., Teukolsky, S.A., Vetterling, W.T., Flannery, B.P., 1992. *Numerical recipes in FORTRAN: The Art of Scientific Computing*, 2nd Edition. Cambridge University Press, Cambridge, 963pp.
- Price, M., Morris, B., Robertson, A., 1982. A study of intergranular and fissure permeability in Chalk and Permian aquifers, using double-packer injection testing. *J. Hydrol.* 54 (4), 401-423. doi.org/10.1016/0022-1694(82)90165-2.
- Quinn, P.M., Parker, B.L., Cherry, J.A., 2011. Using constant head step tests to determine hydraulic apertures in fractured rock. *J. Hydrol.* 126 (1-2), 85-99. doi.org/10.1016/j.jconhyd.2011.07.002.
- Quinn, P., Cherry, J.A., Parker, B.L., 2015. Combined use of straddle packer testing and FLUTE profiling for hydraulic testing in fractured rock boreholes. *J. Hydrol.* 524, 439-454. doi.org/10.1016/j.jhydrol.2015.03.008.
- Quinn, P., Cherry, J.A., Parker, B.L., 2011. Using constant head step tests to determine hydraulic apertures in fractured rock. *J. Hydrol.* 126 (1-2), 85-99. doi.org/10.1016/j.jconhyd.2011.07.002.
- Rehfeldt, K.R., Boggs, J.M., Gelhar, L.W., 1992. Field study of dispersion in a heterogeneous aquifer, 3. Geostatistical analysis of hydraulic conductivity. *Water Resour. Res.* 28 (12), 3309–3324. doi:10.1029/92WR01758.
- Rosa, A.J., Horne, R.N., 1997. Reservoir description by well-test analysis by use of cyclic flow-rate variation. *SPE Formation Evaluation* 12 (04), 247–254. doi:10.2118/22698-PA.
- Ross, H.C., McElwee, C.D., 2007. Multi-Level Slug Tests to Measure 3-D Hydraulic Conductivity Distributions. *Nat. Resour. Res.* 16, 67–79. doi.org/10.1007/s11053-007-9034-9.
- Ruggeri, P., Gloaguen, E., Lefebvre, R., Irving, J., Holliger, K., 2014. Integration of hydrological and geophysical data beyond the local scale: Application of Bayesian sequential simulation to field data from the Saint-Lambert-de-Lauzon site, Québec, Canada. *J. Hydrol.* 514, 271-280. doi.org/10.1016/j.jhydrol.2014.04.031
- Sageev, A., 1986. Slug test analysis. *Water Resour. Res.* 22, 1323–1333.
- Sayler, C., M. Cardiff, and M.D. Fort. 2018. Understanding the geometry of connected fracture flow through multiperiod oscillatory hydraulic testing. *Ground Water* 56(2), 276–287. doi.org/10.1111/gwat.12580
- Shepley, M.G., 2024. Vertical hydraulic conductivity and layered heterogeneity: from measurements to models. *Hydrogeol. J.* 32, 1017–1042. doi.org/10.1007/s10040-024-02773-3

- Sudicky, E.A., Illman, W.A., 2011. Lessons Learned from a Suite of CFB Borden Experiments. *Groundwater* 49, 630-648. doi.org/10.1111/j.1745-6584.2011.00843.x.
- Tiedeman, C.R., Barrash, W., 2020. Hydraulic Tomography: 3D Hydraulic Conductivity, Fracture Network, and Connectivity in Mudstone. *Groundwater* 58, 238-257. <https://doi.org/10.1111/gwat.12915>.
- Tosaka, H., Masumoto, K., Kojima, K., 1993. Hydropulse tomography for identifying 3-D permeability distribution in high level radioactive waste management. In: Proceedings of the Fourth Annual International Conference of the ASCE. Am. Soc. Civ. Eng., Reston, VA, pp. 955–959.
- Tremblay, L., Lefebvre, R., Paradis, D., Gloaguen, E., 2014. Conceptual model of leachate migration in a granular aquifer derived from the integration of multi-source characterization data (St-Lambert, Canada). *Hydrogeol. J.* 22, 587-608. doi.org/10.1007/s10040-013-1065
- Wang, Y.-L., Yeh, T.-C.J., Xu, D., Li, K., Wen, J.-C., Huang, S.-Y., Wang, W., Hao, Y., 2021. Stochastic analysis of oscillatory hydraulic tomography. *Journal of Hydrology*, 596, 10.1016/j.jhydrol.2021.126105
- Yin, M., Ma, R., Zhang, Y., Lin, J., Guo, Z., Zheng, C., 2023. Competitive control of multiscale aquifer heterogeneity on solute transport in an alluvial aquifer. *J. Hydrol.* 616, 128819. doi.org/10.1016/j.jhydrol.2022.128819.
- Zha, Y., Yeh, T.-C.J., Mao, D., Yang, J., Lu, W., 2014. Usefulness of flux measurements during hydraulic tomographic survey for mapping hydraulic conductivity distribution in a fractured medium. *Adv. Water Resour.* 71, 162-176. doi.org/10.1016/j.advwatres.2014.06.008
- Zeyrek, C., Mittelstet, A.R., Gilmore, T.E., Zlotnik, V., Solomon, D.K., Genereux, D.P., Humphrey, C.E., Shrestha, N., 2023. Modeling groundwater transit time distributions and means across a Nebraska watershed: Effects of heterogeneity in the aquifer, riverbed, and recharge parameters. *J. Hydrol.* 617, 128891. doi.org/10.1016/j.jhydrol.2022.128891.

Field deployment and analysis of hydraulic tomography experiments with periodic slug tests in an anisotropic littoral aquifer

Aymen Nefzi, Daniel Paradis, René Lefebvre, Olivier Bour & Nicolas Lavenant

Figures

Journal Pre-proofs

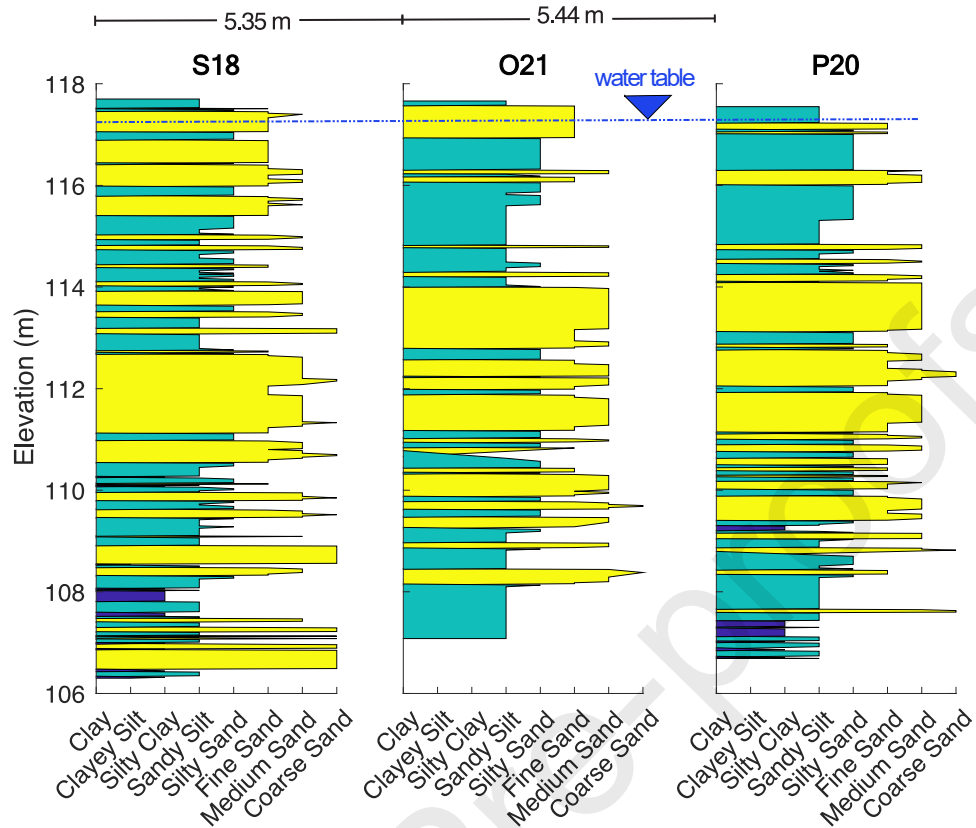


Figure 1. Synthetic lithologic profiles derived from the mechanical properties of cone penetrometer soundings illustrating the heterogeneity of the test site (Paradis et al. 2014). Soundings were taken at the exact same locations where the wells were installed afterward. The locations of the soundings can be found in Figure 3.

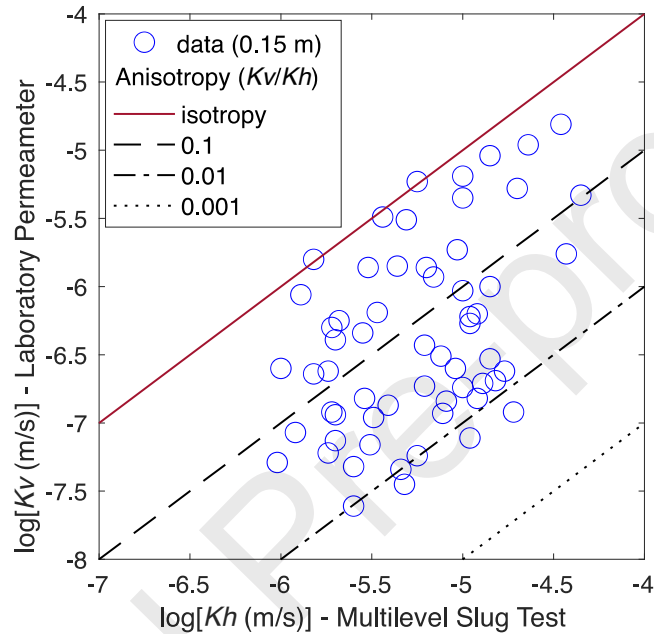


Figure 2. Comparison of horizontal hydraulic conductivity (K_h) estimated using multilevel slug tests with vertical hydraulic conductivity (K_v) estimated on sediment samples using lab permeameter tests as described by Paradis et al. (2014). The length of the test intervals for slug tests and soil samples was 0.15 m. The intervals and samples were at the same depth, with well and sediment sample locations within 1 m of each other. Data was collected at various locations in the study area, including the tomography test site.

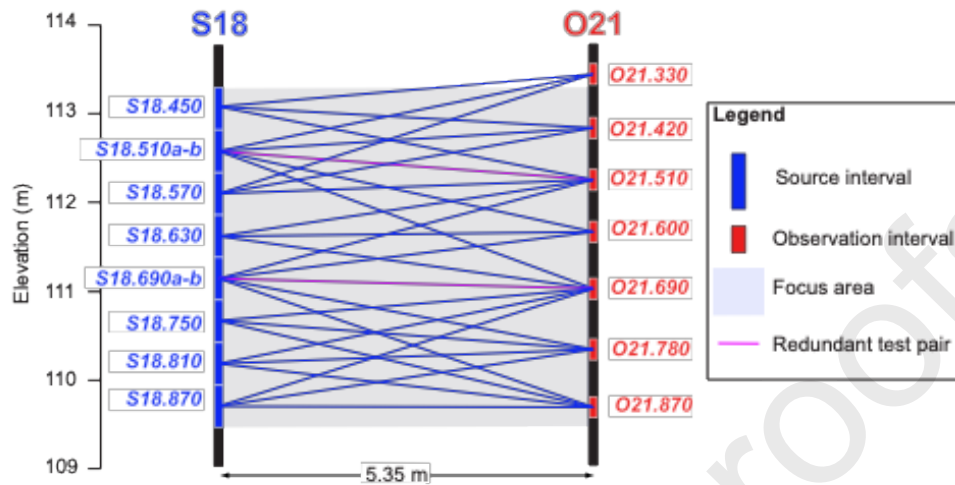


Figure 3. Spatial arrangement of wells at the test site. Configuration of the source and observation intervals (blue lines) used for the tomography experiments between the source well S18 and the observation well O21. The suffixes after the well names indicate the depth of the top of the screens in centimeter with respect to the well collar. The designations S18.510a-b and S18.690a-b indicate that these intervals were tested twice with different configurations of the observation intervals in O21.

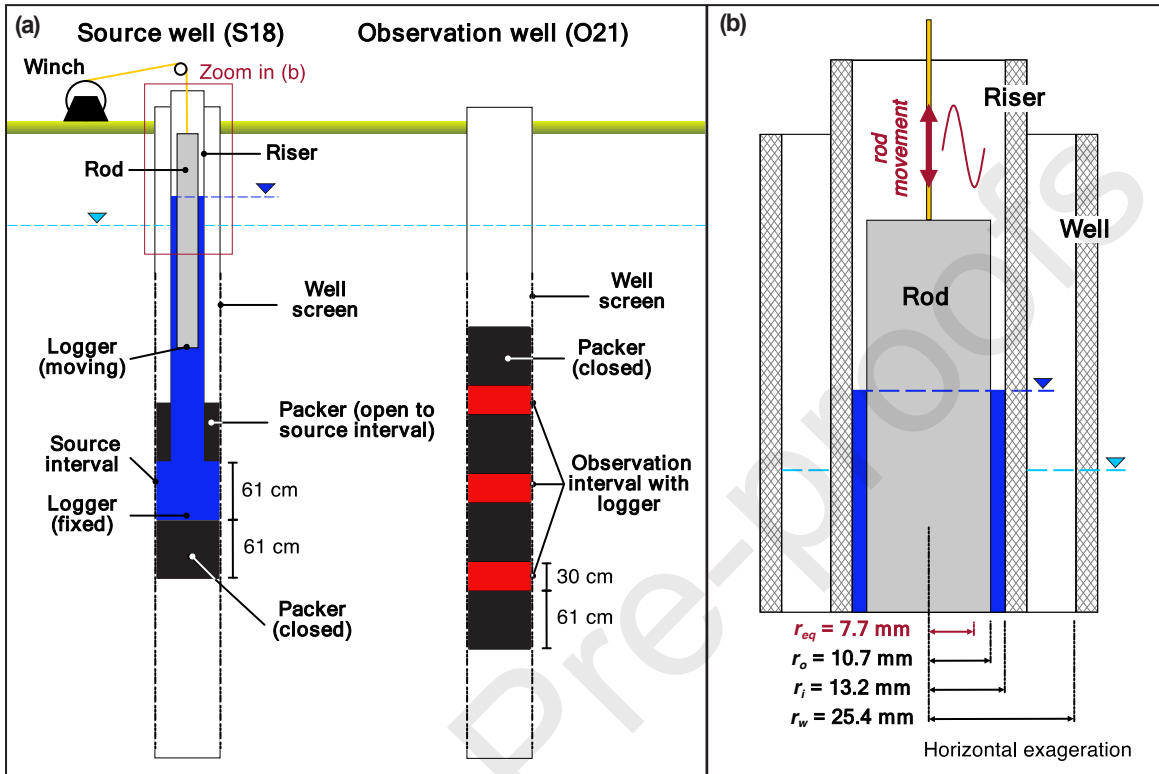


Figure 4. (a) Schematic representation of the packer configurations used for the tomography experiments. (b) Cross-section of the source well, riser tube and rod arrangement with their corresponding radius.

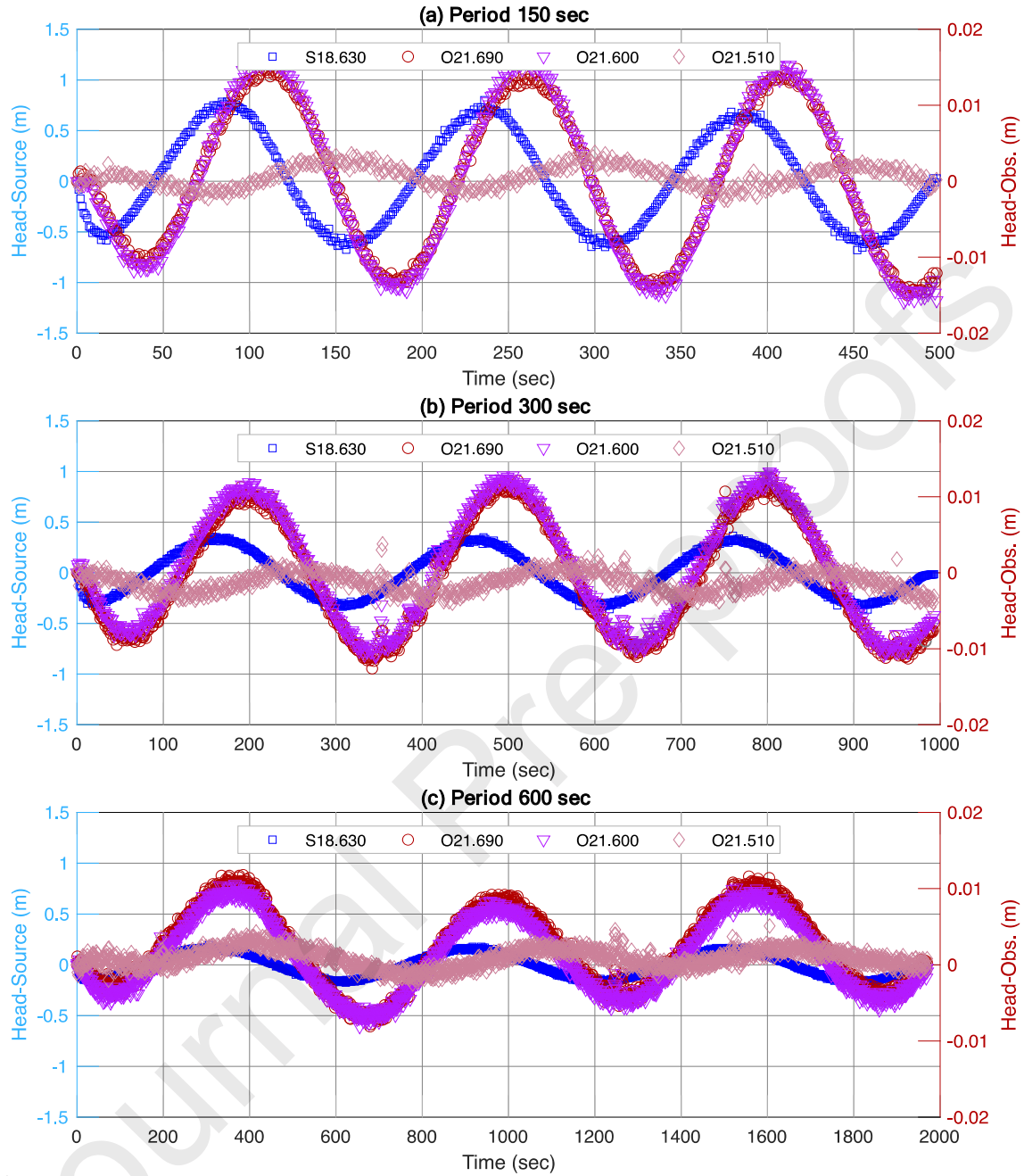


Figure 5. Example of head recordings in the source interval and the three observation intervals for test S18.630 for periods of: (a) 150 s; (b) 300 s; and (c) 600 s. The head represents the variation of the head with respect to the static head measured before each test.

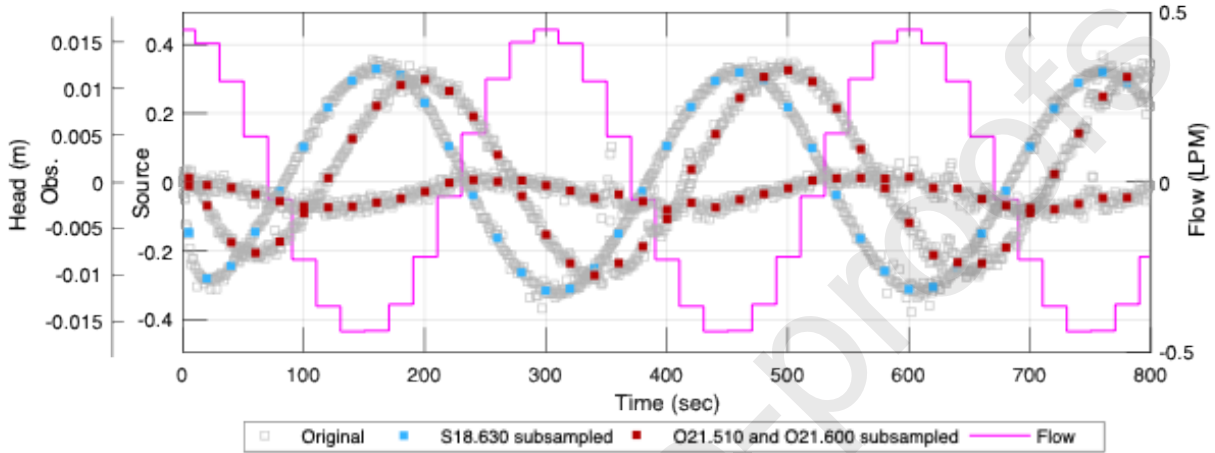


Figure 6. Examples of subsampled head recordings for the source interval S18.630 and two observation intervals (O21.510 and O21.600) for the period of 300 s in relation to the original measurements. An example of a step function representing the modeled flow induced by the rod (Q in liters/minute-LPM) for the numerical simulation is also shown. A positive flow indicates that pumping is taking place (or that the rod is moving upwards).

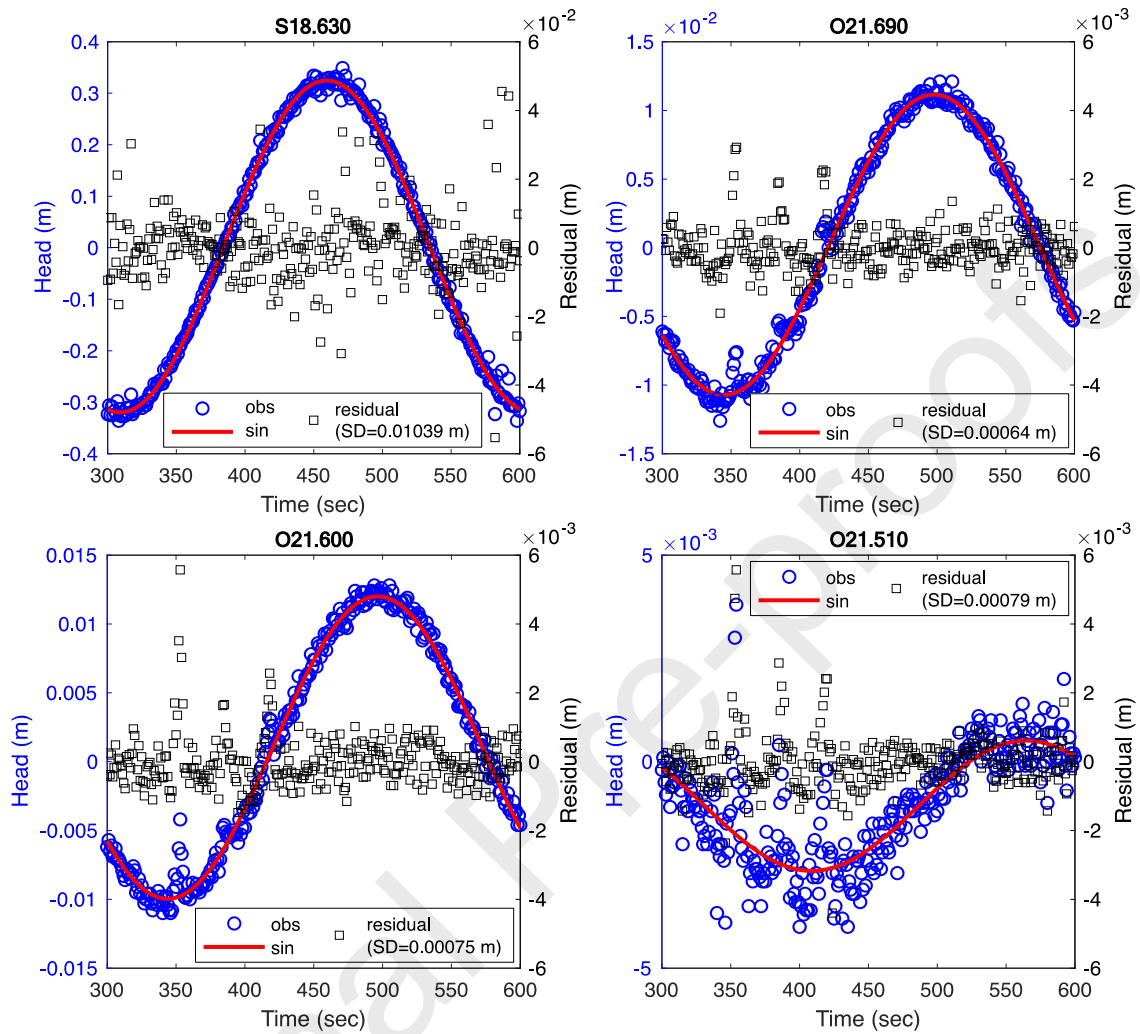


Figure 7. Example of noise level estimation using field data for test S18-630 with a period of 300 s at the source interval (S18.630) and three observation intervals (O21.690, O21.600, and O21.510). The standard deviation (SD) of the residuals is given in the legend.

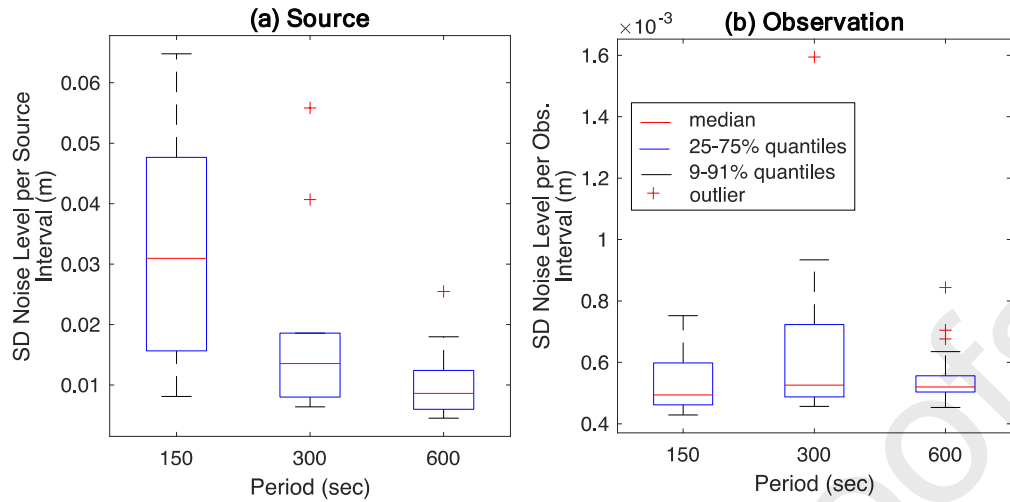


Figure 8. Statistical distribution of the standard deviation of the noise level (residual between the sinusoid and the measurements) per period for the (a) source and the (b) observation intervals. The statistical distributions are determined from the residuals for all individually evaluated source and observation intervals.

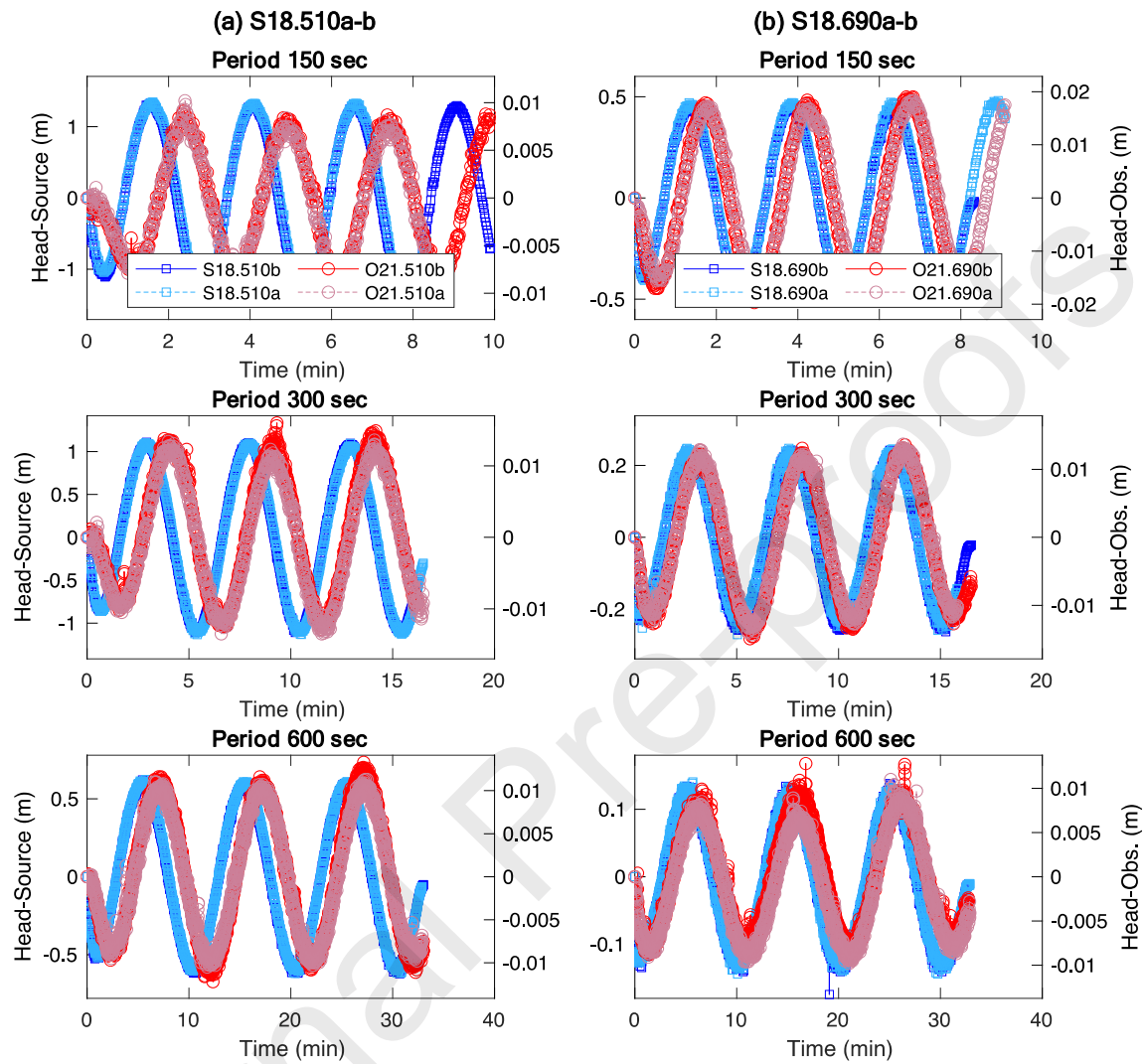


Figure 9. Comparison of the head records for redundant observation intervals (a) O21.510 and (b) O21.690 for tests S18.510a-b and S18.690a-b, respectively.

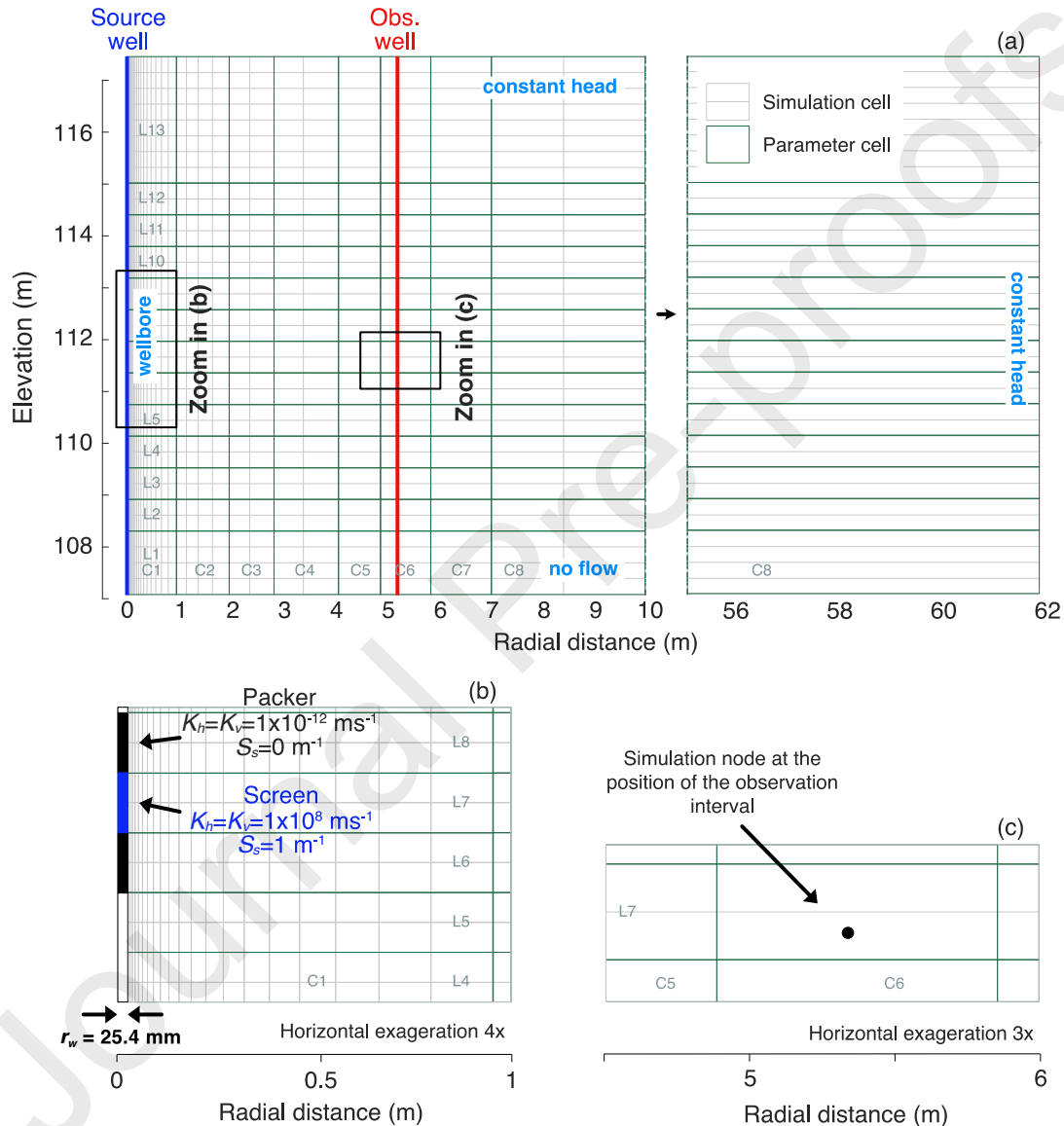


Figure 10. (a) Simulation and parameter grids used for the inversion of the tomography experiments with the relative locations of the wells and boundary conditions. (b) Close-up at the source well showing the position and hydraulic properties of the packers and the screen (packers and screens are integrated in the model). (c) Close-up around the observation well at the position of an observation interval (packers and screens are not explicitly integrated in the model).

Journal Pre-proofs

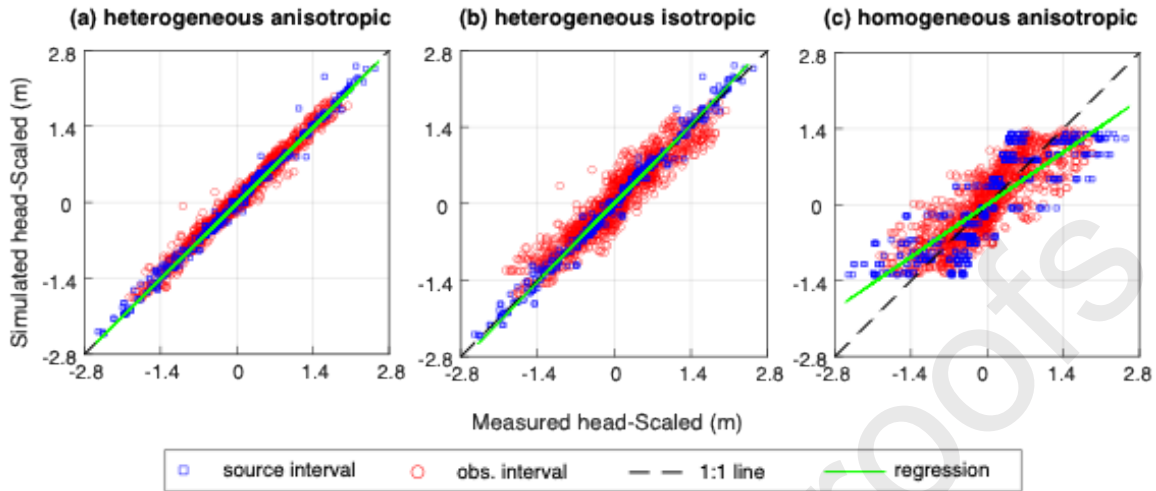


Figure 11. Scatter plots of simulated versus measured heads for all tests of the inversion with the 300-sec period for a (a) heterogeneous and anisotropic model (2b in Table 4), (b) heterogeneous and isotropic model and (c) homogeneous and anisotropic model (2a in Table 4). The homogeneous model (c) was used to obtain the initial hydraulic properties of the heterogeneous and anisotropic model (a). Heads are scaled according to the scaling factors in Section 5.3.

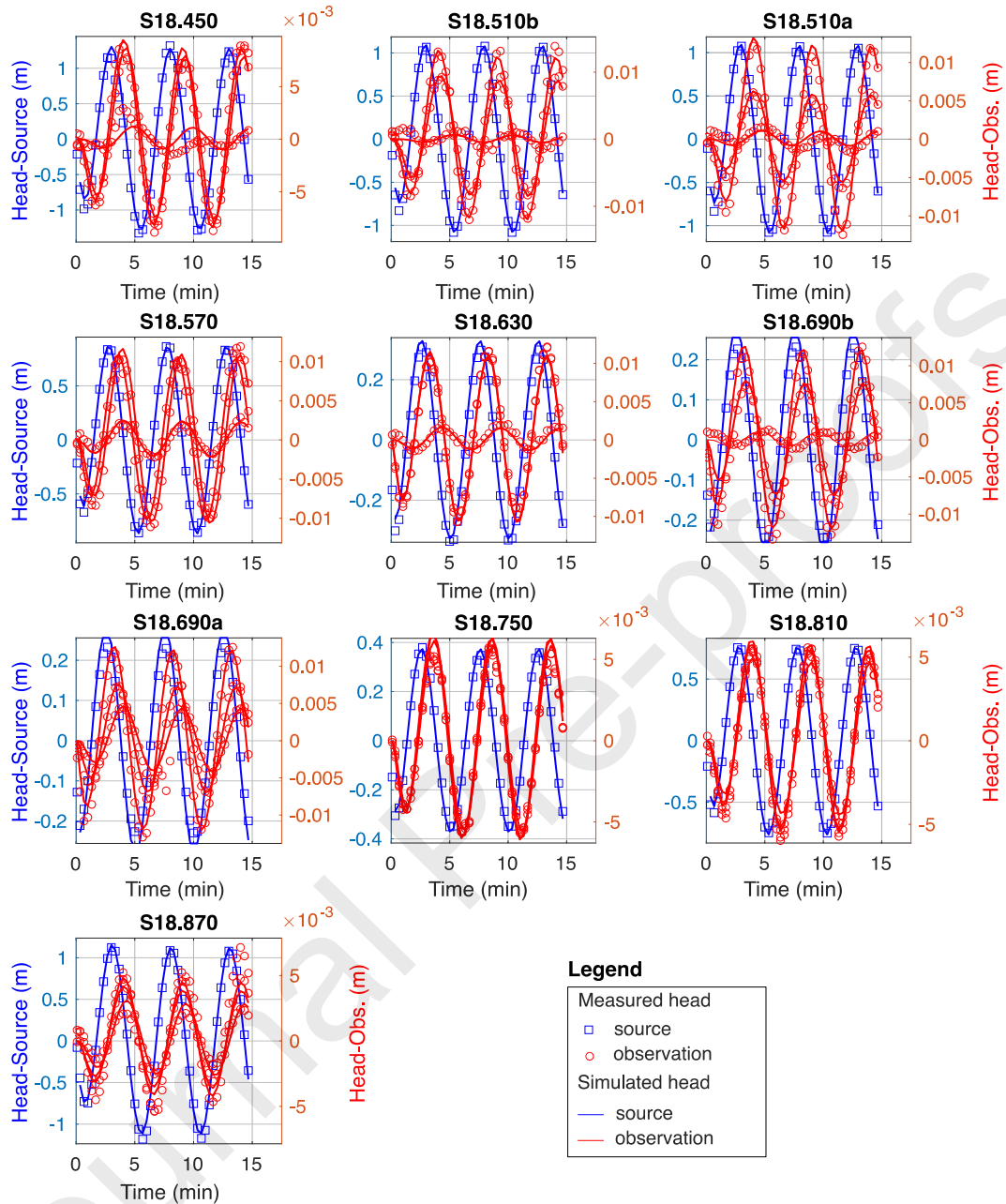


Figure 12. Comparison of the measured and simulated heads for the inversion with the 300-sec period. Data from the intervals of the source (left) and the observation (right) are shown on different scales.

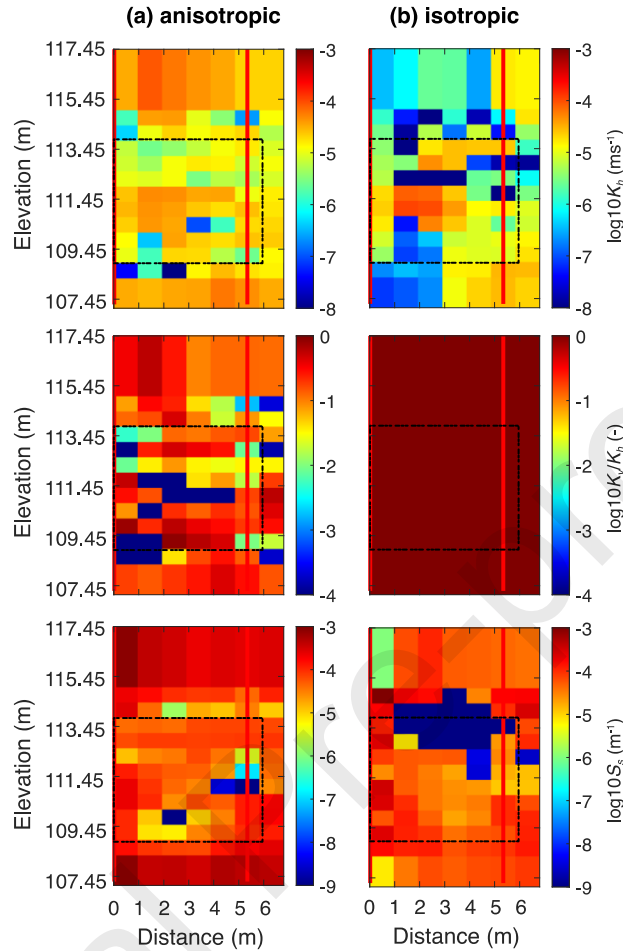


Figure 13. Tomograms for K_h , K_v/K_h and S_s resulting from the inversion of the periodic tests with the 300-sec period under (a) anisotropic and (b) isotropic conditions. The same simulation and parameter grids were used for (a) and (b) (Figure 10), but the inversion of (b) was performed by fixing $K_v/K_h=1$. The rectangle outlined by a black dashed line is the focus area.

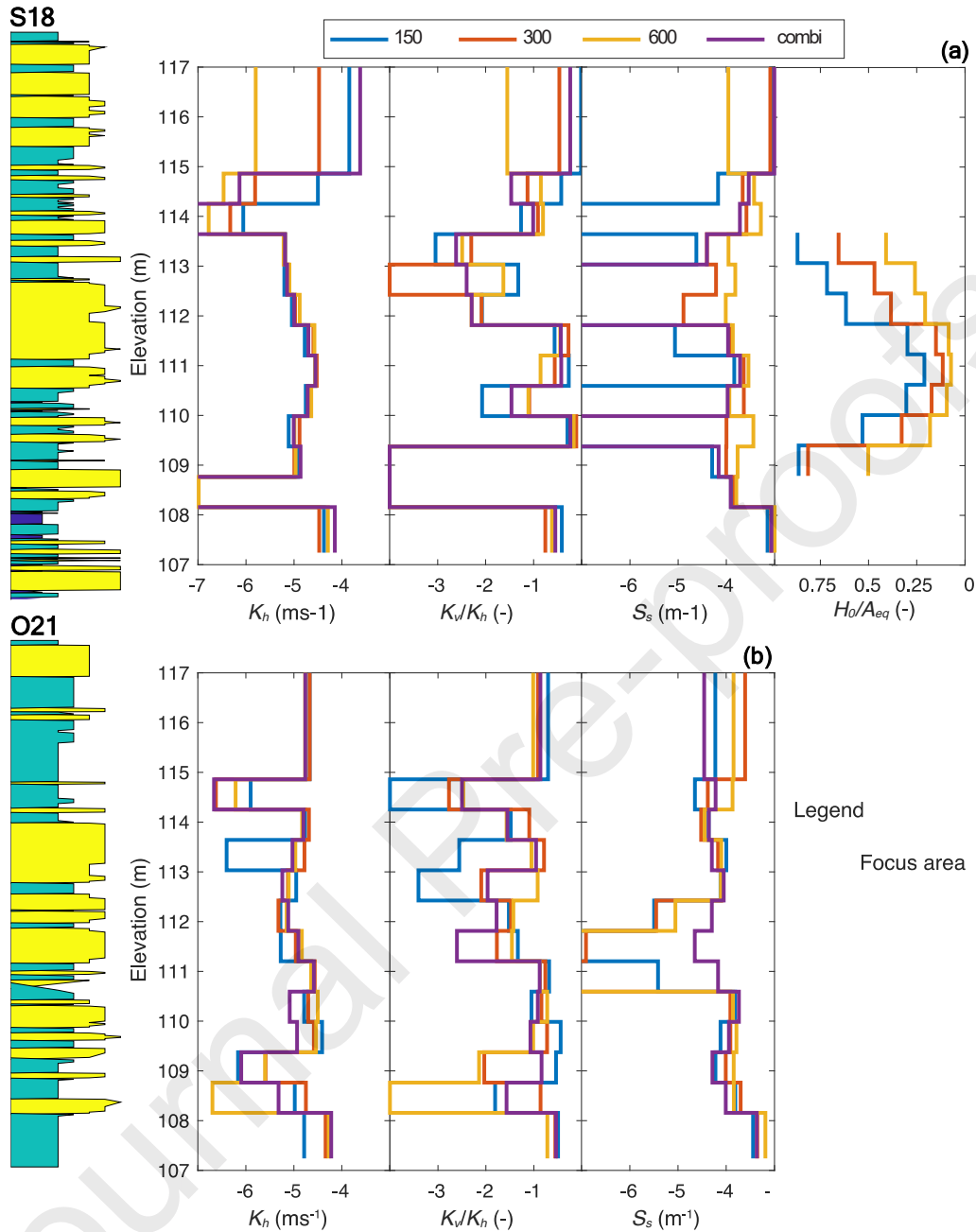


Figure 14. Profiles of hydraulic properties obtained from the inversions of the four heterogeneous simulations in Table 4 with the synthetic geologic logs from cone penetrometer tests along the (a) source well and (b) observation well. The ratio of H_0/A_{eq} in Table 2 is also plotted along the source well. The legend of the geologic logs can be found in Figure 1. The focus area between the upper and lower intervals is highlighted in gray.

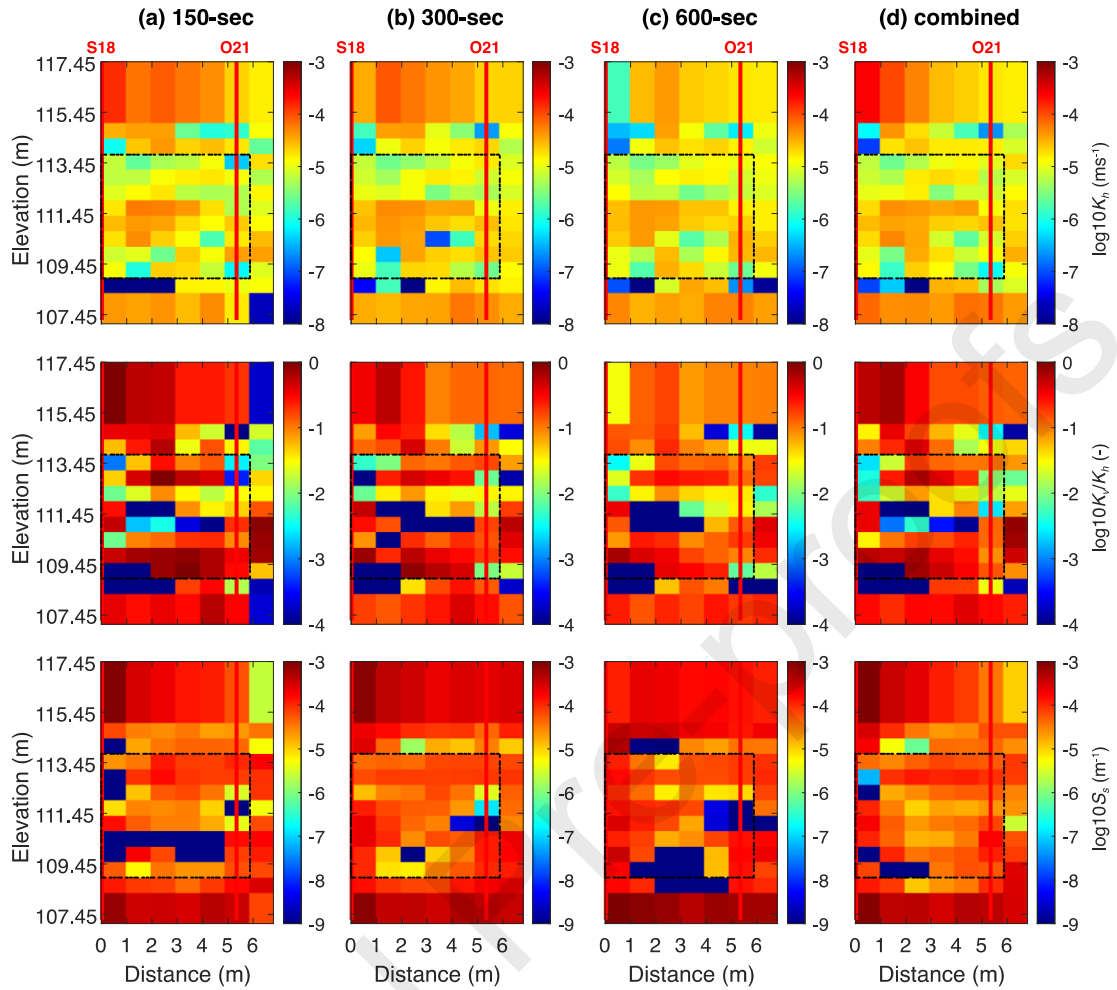


Figure 15. Tomograms for K_h , K_v/K_h , and S_s resulting from the inversion of the periodic tests with the individual period of (a) 150-sec, (b) 300-sec, (c) 600-sec, and (d) the combination of the three periods. The rectangle outlined by a black dashed line is the focus area.

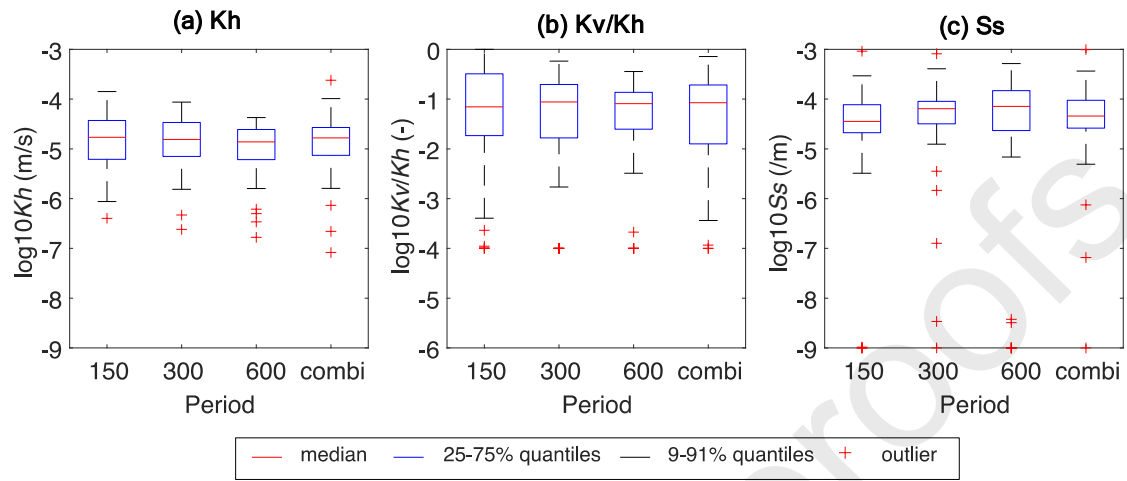


Figure 16. Statistical distribution of the values of (a) Kh, (b) Kv/Kh, and (c) Ss within the focus area resulting from the inversion of the periodic tests with the three individual periods and their combination (combi).

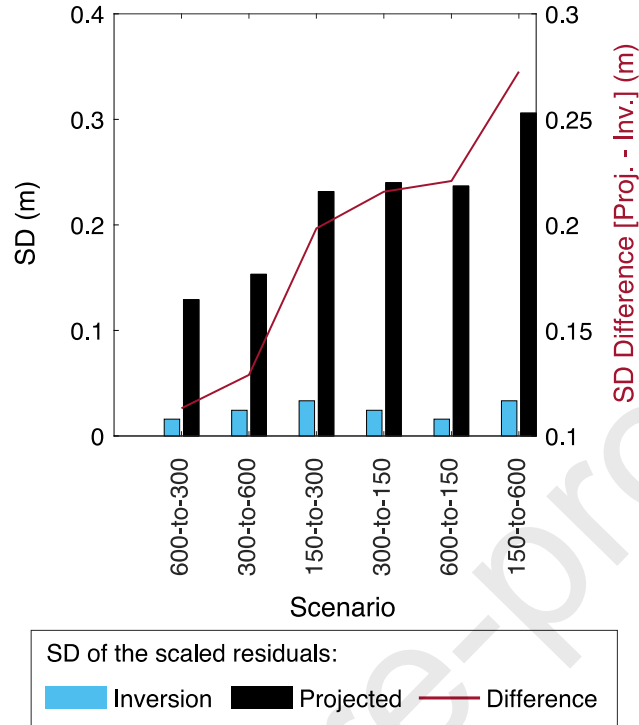


Figure 17. Results of the cross-verification procedure for the six scenarios with individual periods (Table 6). The standard deviation (SD) of the scaled residuals between the inverted and projected models is shown along with their difference. The scenarios are ordered by the ascending value of the difference of the standard deviation. The first number in the scenario name indicates the period of flow and the head used in the simulation, while the last string indicates the model of hydraulic properties.

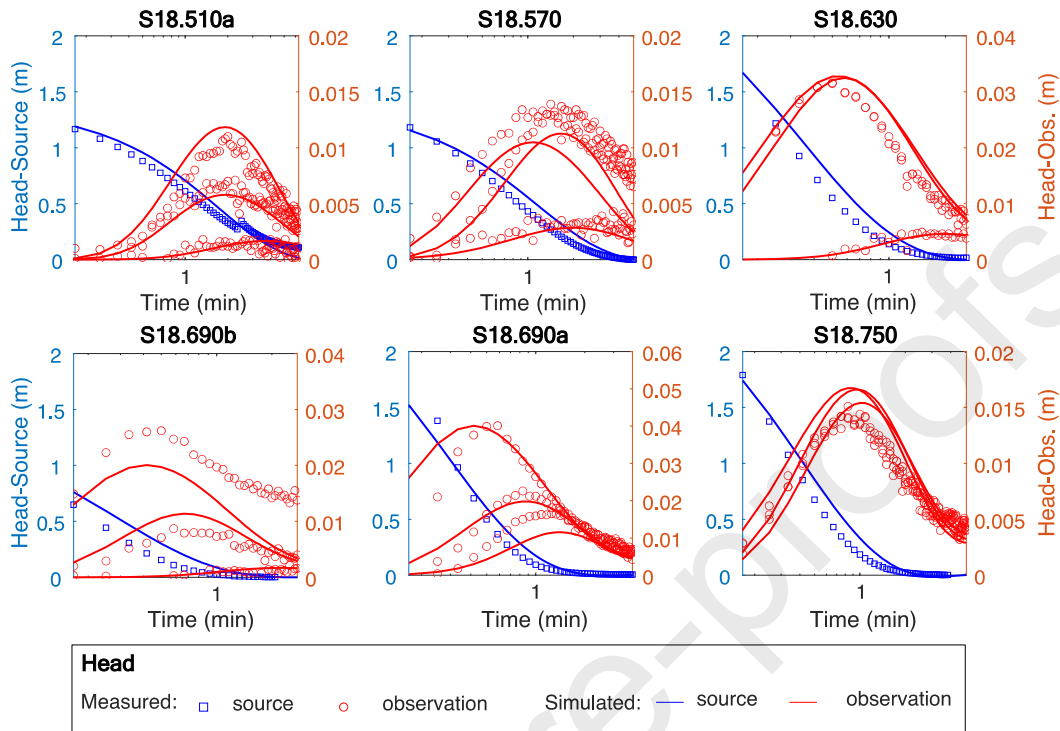


Figure 18. Results of the verification procedure using conventional slug test data that were simulated using the parameter fields obtained from the inversion of measurements with the 300-sec period. (Table 7). Observations and simulations of the source (left scale) and observation (right scale) intervals are shown at different scales. The slug tests were performed in the same intervals as the periodic tests, as shown in Figure 3.

Field deployment and analysis of hydraulic tomography experiments with periodic slug tests in an anisotropic littoral aquifer

Aymen Nefzi, Daniel Paradis, René Lefebvre, Olivier Bour & Nicolas Lavenant

Tables

Journal Pre-proofs

Table 1. Description of periodic tests with corresponding sources and observation intervals, test periods, and peak amplitudes corresponding to the displacement of the rod (A_0). Positions of tested intervals is shown in Figure 2. The bold observation intervals indicate redundant tests.

Interval				Period (s)		
				150	300	600
Source	Observation			A_0 (m)		
S18.450	O21.330	O21.420	O21.510	0.85	1.10	1.10
S18.510b	O21.330	O21.420	O21.510	1.00	1.25	1.25
S18.510a	O21.510	O21.600	O21.690	1.00	1.25	1.25
S18.570	O21.510	O21.600	O21.690	1.00	1.25	1.25
S18.630	O21.510	O21.600	O21.690	1.25	1.25	1.25
S18.690b	O21.510	O21.600	O21.690	1.25	1.25	1.25
S18.690a	O21.690	O21.780	O21.870	1.25	1.25	1.25
S18.750	O21.700	O21.790	O21.880	1.25	1.25	1.25
S18.810	O21.700	O21.790	O21.880	1.25	1.25	1.25
S18.870	O21.690	O21.780	O21.870	0.75	0.75	0.75

Table 2. Signals and responses of the periodic tests with the peak amplitude corresponding to the displacement of the rod (A_0), the equivalent variation of the head induced by the rod in the source interval (A_{eq}), the variation of the head measured in the source interval (H_0), and the maximum (h_0 max) and minimum (h_0 min) heads measured in the observation intervals. A_{eq} is defined by Equation (7).

Test	Period (sec)	Peak amplitude (m)					H_0/A_{eq}
		Rod		Interval			
				Source	Observation		
		A_0	A_{eq}	H_0	h_0 max	h_0 min	
S18.450	150	0.85	1.63	1.3855	0.0060	0.0010	0.85
	300	1.10	2.11	1.3379	0.0091	0.0028	0.63
	600	1.10	2.11	0.8262	0.0084	0.0015	0.39
S18.510b	150	1.00	1.92	1.3402	0.0087	0.0017	0.70
	300	1.25	2.40	1.0850	0.0130	0.0017	0.45
	600	1.25	2.40	0.5924	0.0116	0.0014	0.25
S18.510a	150	1.00	1.92	1.3238	0.0089	0.0014	0.69
	300	1.25	2.40	1.0874	0.0131	0.0017	0.45
	600	1.25	2.40	0.5956	0.0102	0.0012	0.25
S18.570	150	1.00	1.92	1.1600	0.0095	0.0019	0.60
	300	1.25	2.40	0.8716	0.0114	0.0026	0.36

	600	1.25	2.40	0.4495	0.0089	0.0021	0.19
S18.630	150	1.25	2.40	0.6820	0.0155	0.0023	0.28
	300	1.25	2.40	0.3261	0.0112	0.0020	0.14
	600	1.25	2.40	0.1631	0.0088	0.0022	0.07
	150	1.25	2.40	0.4498	0.0189	0.0017	0.19
S18.690b	300	1.25	2.40	0.2411	0.0136	0.0014	0.10
	600	1.25	2.40	0.1260	0.0086	0.0017	0.05
	150	1.25	2.40	0.4606	0.0171	0.0057	0.19
S18.690a	300	1.25	2.40	0.2336	0.0131	0.0060	0.10
	600	1.25	2.40	0.1274	0.0096	0.0074	0.05
	150	1.25	2.40	0.6995	0.0063	0.0061	0.29
S18.750	300	1.25	2.40	0.3687	0.0060	0.0058	0.15
	600	1.25	2.40	0.1925	0.0042	0.0042	0.08
	150	1.25	2.40	1.2747	0.0054	0.0052	0.53
S18.810	300	1.25	2.40	0.7584	0.0057	0.0057	0.32
	600	1.25	2.40	0.4065	0.0047	0.0047	0.17
	150	0.75	1.44	1.2199	0.0036	0.0016	0.85
S18.870	300	0.75	1.44	1.1597	0.0064	0.0024	0.80

	600	0.75	1.44	0.6864	0.0069	0.0056	0.48
--	-----	------	------	--------	--------	--------	------

Journal Pre-proofs

Table 3. Median standard deviation (SD) of the residual between a sinusoid and the original head measurements recorded at 1 sample per second. The SD of the subsampled head used for the inversion is also provided. The amount of data for the subsampled data set is the same for all periods and corresponds to 15 measurements per cycle. The median is obtained from the SD of the residuals for all individually evaluated source and observation intervals.

Period (s)	Median SD of the residual (m)			
	Original (1/s)		Subsampled (15/cycle)	
	Source	Obs.	Source	Obs.
150	3.1×10^{-2}	4.9×10^{-4}	2.6×10^{-2}	1.8×10^{-4}
300	1.4×10^{-2}	5.3×10^{-4}	5.9×10^{-3}	1.8×10^{-4}
600	8.6×10^{-3}	5.2×10^{-4}	1.9×10^{-3}	1.4×10^{-4}

Table 4. Simulation program for the inversion of the tomography experiments with different periods. Note that the final hydraulic parameters obtained from the inversion of the homogeneous model (a) are used as initial parameters for the heterogeneous model (b).

Inversion	Period (sec)	Number of test (interval)	a-Homogeneous model for all tests (1 zone)	b-Heterogeneous model for all tests (104 zones)		
			Hydraulic parameters			
			Initial	Final	Initial	Final
1a-b	150	10 (40)		$K_h 1.10 \times 10^{-5} \text{ ms}^{-1}$ $K_v/K_h 1.23 \times 10^{-1}$ $S_s 4.74 \times 10^{-5} \text{ m}^{-1}$	Fig. 15a	
2a-b	300	10 (40)	$K_h 1 \times 10^{-5} \text{ ms}^{-1}$ $K_v/K_h 1 \times 10^{-1}$	$K_h 1.19 \times 10^{-5} \text{ ms}^{-1}$ $K_v/K_h 8.15 \times 10^{-2}$ $S_s 6.88 \times 10^{-5} \text{ m}^{-1}$	Fig. 15b	
3a-b	600	10 (39)	$S_s 1 \times 10^{-5} \text{ m}^{-1}$	$K_h 1.18 \times 10^{-5} \text{ ms}^{-1}$ $K_v/K_h 6.09 \times 10^{-2}$ $S_s 8.00 \times 10^{-5} \text{ m}^{-1}$	Fig. 15c	
4a-b	combi: 150, 300 and 600	30 (119)		$K_h 1.18 \times 10^{-5} \text{ ms}^{-1}$ $K_v/K_h 8.80 \times 10^{-2}$ $S_s 6.12 \times 10^{-5} \text{ m}^{-1}$	Fig. 15d	

Journal Pre-proofs

Table 5. Mean and standard deviation (SD) of the residuals for source and observation intervals for the four inversions. The standard deviation, the coefficient of determination (R^2) and the slope of the linear regression (m) of the scaled residuals are also shown. The scaling factors for the scaled residuals are described in Section 5.3. The runtime is for an ARM-based M1 processor with 16 cores and a clock frequency of 3.2 GHz.

Inversion	Period (s)	Runtime (min)	Residuals				Scaled Residuals		
			Source		Observation		Source and Observation		
			Mean (m)	SD (m)	Mean (m)	SD (m)	SD (m)	R^2 (-)	m (-)
1b	150	102	-3.5×10^{-3}	6.6×10^{-2}	-3.7×10^{-4}	7.2×10^{-4}	3.3×10^{-2}	0.996	0.965
2b	300	80	-5.3×10^{-3}	4.8×10^{-2}	-2.0×10^{-4}	8.0×10^{-4}	2.4×10^{-2}	0.996	0.998
3b	600	91	-4.0×10^{-4}	3.1×10^{-2}	-1.2×10^{-4}	8.8×10^{-4}	1.6×10^{-2}	0.995	1.000
4b	combi	374	-7.0×10^{-4}	5.1×10^{-2}	-1.6×10^{-4}	9.4×10^{-4}	3.5×10^{-2}	0.990	0.980

Table 6. Mean, standard deviation (SD), coefficient of determination (R^2) and slope of the linear regression (m) of the scaled residuals for the nine cross-verification simulations. The SD of the original inversion and its difference with the cross-verification simulation are also shown. A negative value of the mean indicates that the simulated head is overestimated compared to the measurements. The color scale for the columns of SD is red for the maximum and green for the minimum. The first number in the simulation name indicates the period for the flow rate and the head used in the simulation, while the last string indicates the model of hydraulic properties.

Simulation	Scaled Residuals					
	Inversion	Cross-Verification				Difference
	SD (m)	Mean (m)	SD (m)	R^2 (-)	m (-)	SD (m)
150-to-300	3.3×10^{-2}	-2.8×10^{-2}	2.3×10^{-1}	0.98	0.80	2.0×10^{-1}
150-to-600	3.3×10^{-2}	-2.2×10^{-2}	3.1×10^{-1}	0.98	0.72	2.7×10^{-1}
300-to-150	2.4×10^{-2}	-4.5×10^{-2}	2.4×10^{-1}	0.98	1.16	2.2×10^{-1}
300-to-600	2.4×10^{-2}	-2.1×10^{-2}	1.5×10^{-1}	0.99	0.91	1.3×10^{-1}
600-to-150	1.6×10^{-2}	-3.3×10^{-2}	2.4×10^{-1}	0.96	1.19	2.2×10^{-1}
600-to-300	1.6×10^{-2}	-1.5×10^{-2}	1.3×10^{-1}	0.98	1.00	1.1×10^{-1}
150-to-combi	3.5×10^{-2}	-3.4×10^{-2}	1.5×10^{-1}	0.99	0.90	1.1×10^{-1}
300-to-combi	3.5×10^{-2}	-3.0×10^{-2}	1.3×10^{-1}	0.99	1.03	1.0×10^{-1}
600-to-combi	3.5×10^{-2}	-1.8×10^{-2}	1.3×10^{-1}	0.98	1.02	1.0×10^{-1}

Journal Pre-proofs

Table 7. Descriptive statistics (mean, standard deviation-SD, coefficient of determination- R^2 and slope of the linear regression- m) of the scaled residuals for the verification simulations of conventional slug tests with the parameter fields inverted from individual and combined oscillatory tomographic experiments.

Simulation	Scaled Residuals			
	Mean (m)	SD (m)	R^2 (-)	m (-)
150	-2.5×10^{-2}	9.7×10^{-2}	0.93	1.15
300	-8.6×10^{-3}	7.2×10^{-2}	0.95	1.02
600	-8.2×10^{-3}	7.4×10^{-2}	0.94	1.01
combi	-1.5×10^{-2}	8.3×10^{-2}	0.94	1.09

Field deployment and analysis of hydraulic tomography experiments with periodic slug tests in an anisotropic littoral aquifer

Aymen Nefzi¹, Daniel Paradis², René Lefebvre¹, Olivier Bour³ & Nicolas Lavenant³

¹ Centre Eau Terre Environnement (INRS-ETE) - Institut national de la recherche scientifique, Québec, Canada

² Ressources Naturelles Canada - Commission géologique du Canada, Québec, Canada

³ Université Rennes, CNRS, Géosciences Rennes, UMR 6118, 35000 Rennes, France

Highlights

1. Hydraulic tomography with periodic signals is applied in a littoral aquifer
2. Thirty slug tests with three periods reveal significant aquifer heterogeneity
3. Joint inversion with flow rate and head estimates hydraulic conductivity anisotropy
4. Tests from different periods yield similar models of hydraulic properties
5. This study identifies future research directions to enhance hydraulic tomography

Field deployment and analysis of hydraulic tomography experiments with periodic slug tests in an anisotropic littoral aquifer

Aymen Nefzi¹, Daniel Paradis², René Lefebvre¹, Olivier Bour³ & Nicolas Lavenant³

¹ Centre Eau Terre Environnement (INRS-ETE) - Institut national de la recherche scientifique, Québec, Canada

² Ressources Naturelles Canada - Commission géologique du Canada, Québec, Canada

³ Université Rennes, CNRS, Géosciences Rennes, UMR 6118, 35000 Rennes, France

Abstract

Accurate mapping of the heterogeneity of hydraulic properties, including hydraulic conductivity (K_h) and its anisotropy (K_v/K_h), is crucial for predicting groundwater flow and solute transport in aquifers. This study investigates the use of hydraulic tomography with periodic signals to map K_h , K_v/K_h and specific storage (S_s) in an unconsolidated littoral aquifer. The periodic signals were generated by the movement of a rod numerically controlled by a winch, which allowed the signal amplitude and period to be imposed. Thirty periodic slug tests with periods of 150, 300 and 600 seconds were conducted between isolated intervals in a source well and an observation well, generating 120 head responses. Numerical inversion in the time domain used the rod-induced flow rates and associated heads to estimate the heterogeneous fields. Significant

differences in head amplitude and phase shift between test intervals at different locations highlighted the heterogeneity of the aquifer. The inversion results for single and combined periods are consistent with the values of previous studies and the heterogeneous nature of the littoral aquifer. Comparison of models from different periods revealed slight spatial and statistical variations in hydraulic properties and different hydraulic behavior when tested with independent hydraulic tests. While the fundamentals of understanding the information in the different periodic signals need to be further clarified, this study advances the application of hydraulic tomography under real field conditions and highlights its effectiveness in characterizing aquifer heterogeneity and anisotropy.